

BETIS: Bidimensional Exploration of the warm-Temperature Ionised gaS

I. Sample presentation and first results

R. González-Díaz^{1,2} , F. F. Rosales-Ortega² , L. Galbany^{1,3} , J. P. Anderson^{4,5} , C. Jiménez-Palau¹ , M. Kopsacheili¹ , H. Kuncarayakti^{8,9} , J. D. Lyman⁶ , and S. F. Sánchez⁷ 

¹ Institute of Space Sciences (ICE-CSIC), Campus UAB, Carrer de Can Magrans, s/n, E-08193 Barcelona, Spain.
e-mail: Raul.GonzalezD@autonoma.cat

² Instituto Nacional de Astrofísica, Óptica y Electrónica (INAOE-CONAHCyT), Luis E. Erro 1, 72840 Tonantzintla, Puebla, México.

³ Institut d'Estudis Espacials de Catalunya (IEEC), E-08034 Barcelona, Spain.

⁴ European Southern Observatory, Alonso de Córdova 3107, Vitacura, Casilla 19001, Santiago, Chile.

⁵ Millennium Institute of Astrophysics MAS, Nuncio Monseñor Sotero Sanz 100, Off. 104, Providencia, Santiago, Chile.

⁶ Department of Physics, University of Warwick, Coventry CV4 7AL, UK.

⁷ Instituto de Astronomía, Universidad Nacional Autónoma de México, A. P. 70-264, C.P. 04510, Ciudad de México, México.

⁸ Finnish Centre for Astronomy with ESO (FINCA), FI-20014 University of Turku, Finland.

⁹ Tuorla Observatory, Department of Physics and Astronomy, FI-20014 University of Turku, Finland.

Received ... ; accepted ...

ABSTRACT

We present the Bidimensional Exploration of the warm-Temperature Ionised gaS (BETIS) project, designed for the spatial and spectral study of the Diffuse Ionised Gas (DIG) in a selection of 265 nearby spiral galaxies observed with MUSE. Our primary objective is to investigate the various ionisation mechanisms at play within the DIG by analysing the distribution of high- and low-ionisation species in the optical spectra of the sample. This sample encompasses different morphological types and spans a stellar mass range between 10^8 and $10^{12} M_{\odot}$, within a redshift < 0.06 featuring a spatial resolution varying from 41 pc to 1.6 kpc, and an average of 275 pc. We introduce a new methodology for defining the DIG. Firstly, we employ an innovative adaptive binning technique on the observed datacube based on the spectroscopic signal-to-noise ratio (SN) of the collisional [S II] line, in order to increase the SN of the rest of the lines including [O III], [O I], and He I. Subsequently, we create a DIG mask by eliminating the emissions associated with both bright and faint H II regions. We also examine the suitability of using $H\alpha$ equivalent width ($EW(H\alpha)$) as a proxy for defining the DIG and its associated ionisation regime. Notably, for $EW(H\alpha) < 3\text{\AA}$ – the expected emission from hot low-mass evolved stars (HOLMES) – the measured value is contingent on the chosen population synthesis technique performed. Our analysis in a showcase subsample reveals a consistent cumulative DIG fraction across all galaxies in the subsample, averaging around 40%-70%. The average radial distribution of the [N II]/ $H\alpha$, [S II]/ $H\alpha$, [O I]/ $H\alpha$ and [O III]/ $H\beta$ ratios are enhanced in the DIG regimes (up to 0.2 dex), and follows similar trends between the DIG regime and the H II regions, as well as $H\alpha$ surface brightness ($\Sigma_{H\alpha}$), indicating a correlation between the ionisation of these species in both the DIG and the H II regions. The DIG loci in typical diagnostic diagrams are found, in general, within the line ratios that correspond to photoionisation due to the star formation. There is a noticeable offset correspondent to ionisation due to fast shocks. However, an individual diagnosis performed for each galaxy reveals that all the DIG in these galaxies can be attributed to photoionisation from star formation. The offset is primarily due to the contribution of the two Seyfert galaxies in our subsample, which closely align with models of ionisation from fast shocks, thus mimicking the DIG emission. Consequently, this offset should be disregarded when conducting a global DIG diagnosis.

Key words. galaxies: ISM – galaxies: star formation – H II regions – ISM: structure – ISM: general

1. Introduction

Understanding the relationship between stellar formation processes and the interstellar medium (ISM) is a key step in discerning the complexity in the evolutionary history of galaxies. A problem in this regard has been understanding the nature and importance of feedback processes in which massive stars deposit energy into the interstellar medium through photoionisation, stellar winds, and supernovae. This feedback mechanism affects the physical and dynamic state of the ISM and therefore has an influence on the rate and distribution of stellar formation in galaxies (Ceverino & Klypin 2008, 2009; Hopkins et al. 2014; Klessen & Glover 2016; Gatto et al. 2017; Grisdale 2017).

In this context, the existence of a warm and ionised component of the ISM that is ubiquitously distributed in our galaxy has been known for decades (Hoyle & Ellis 1963; Hewish et al. 1968; Guélin 1974), this component of the Milky Way was called warm ionised medium (WIM) (Reynolds 1971; Reynolds et al. 1973; Reynolds 1985, 1989; Kennicutt et al. 1989; Finkbeiner 2003). With the warm temperatures and low densities found in this medium ($0.6 - 1 \cdot 10^4$ K and $\sim 10^{-1} \text{cm}^{-3}$ respectively, with an emission measure of $\sim 35 \text{cm}^{-6} \text{pc}$), the WIM represents the 20% of the ISM in volume and the 90% of the ionising hydrogen in mass, being one of the most important components of our galaxy (Reynolds 1971; Monnet 1971). The intensity of the for-

bidden [S II] $\lambda 6716$ and [N II] $\lambda 6584$ lines is found to be higher with respect to the $H\alpha$ intensity in the WIM in comparison with the typical intensities of the H II regions, besides, the measure of these lines reveals that the ionisation state of the WIM and its temperature vary significantly along the galactic plane, increasing towards the galactic center (Reynolds 1985; Madsen & Reynolds 2005). Moreover, the filling fraction increases as the height with respect to the galactic plane increases, being around 0.1 at the midplane and reaching 0.3-0.4 at 1 kpc from the galactic plane (Kulkarni & Heiles 1987; Reynolds 1991; Berkhuijsen et al. 2006; Gaensler et al. 2008).

The first detections of this medium in other galaxies, now referred as diffuse ionised gas (DIG) in the extragalactic context, were carried out through narrowband $H\alpha$ images of edge-on star-forming galaxies (Rand et al. 1990; Dettmar 1990). This was followed up by studies carried by small samples (<5) of face-on and edge-on galaxies using narrowband $H\alpha$ and [S II] images (Ferguson et al. 1996a; Greenawalt et al. 1997; Zurita et al. 2000) and long-slit spectroscopy with limited spatial coverage (Reynolds 1985; Wang et al. 1997; Otte et al. 2001; Hoopes & Walterbos 2003; Haffner et al. 2009a).

All these studies have shown that 30%–50% of the total $H\alpha$ luminosity of their galaxies correspond to the DIG, being the $80 \pm 10\%$ of the projected area of the disks occupied by DIG (Oey et al. 2007), thereby proving the ubiquitousness and omnipresence of this component in the star-forming galaxies. Moreover, the spectroscopic studies shown that the emission of low-ionisation lines, such as [S II] $\lambda\lambda 6717, 31$, [N II] $\lambda 6584$ or [O I] $\lambda 6300$, are enhanced in DIG/WIM regimes in comparison with the emission of the H II regions (Wang et al. 1997). Specifically, the ratios of those lines with respect the $H\alpha$ emission in the DIG are larger than in H II regions (found firstly in edge-on galaxies; Otte et al. 2001). The leakage of the Ly α photons, produced by the OB stars within H II regions, is commonly regarded as the primary source of DIG/WIM ionisation (Haffner et al. 2009b; Seon 2009; Belfiore et al. 2022). However, it has been observed that, in some cases, the total energy output of these stars does not appear to provide the necessary power to ionize the DIG uniformly across galactic discs (Ferguson et al. 1996a,b). The substantial power demand, combined with the presence of high-ionisation species like [O III] (enhanced at more than 1 kpc above the galactic plane) and He I (Reynolds et al. 1998; Wood & Mathis 2004; Haffner et al. 2009b) underscores the insufficiency of Ly α photons leaking from H II regions in explaining the existence of the DIG. The question of the ionisation source for this component continues to be a topic of ongoing debate, with numerous proposals suggesting alternative heating sources for the DIG. Some of these sources include photoelectric heating from interstellar dust particles or large molecules (Reynolds & Cox 1992; Weingartner & Draine 2001), fast shocks provided by Wolf-Rayet stars or supernovae (Reynolds et al. 1998; Collins & Rand 2001; Hidalgo-Gómez 2005), turbulent mixing layers and dissipation of turbulence (Slavin et al. 1993; Minter & Spangler 1997; Reynolds et al. 1998; Binette et al. 2009), cosmic ray heating (Wiener et al. 2013) or microflares and magnetic field reconnections (Raymond 1992; Birk et al. 1998). Another alternative source of ionisation, as proposed by Flores-Fajardo et al. (2011) and Cid Fernandes et al. (2011), is the photoionisation from hot low-mass evolved stars (HOLMES), that could provide an explanation for the high [O III]/ $H\alpha$ ratio observed in the extraplanar DIG (Rand et al. 1990).

The extent to which HOLMES contribute to the ionising radiation responsible for the DIG remains uncertain. While they may play a role in ionising specific regions within the sparsely

populated interstellar medium, their overall significance is not yet established. Initial calculations conducted by Hills (1974) proposed that the ionising radiation emitted by these hot pre-white dwarf stars could have a substantial influence on the interstellar medium.

The exploration of the combination of Ly α photon leakage and HOLMES as potential primary sources of ionisation for the DIG has been extensively investigated using integral field spectrographs (IFS). The IFS offers simultaneous spatial and spectral information, enabling the examination of these ionisation mechanisms across a wide range of spatial resolutions and high spectral resolution. Some IFS surveys provides large samples of nearby galaxies at kiloparsec resolution such as the Calar Alto Legacy Integral Field spectroscopy Area survey (CALIFA; Sánchez et al. 2012; Husemann et al. 2013; 391 galaxies at ~ 0.8 kpc resolution; Lacerda et al. 2018, hereafter Lac18) or the Mapping Nearby Galaxies at APO (MaNGA; Bundy et al. 2015; 356 galaxies at 2 kpc resolution; Zhang et al. 2017, hereafter Z17).

Z17 found an enhancement in the DIG of the ratios [S II]/ $H\alpha$, [N II]/ $H\alpha$, [O II]/ $H\alpha$ and [O I]/ $H\alpha$, increasing in function of the galactocentric radius, as well as a variable trend of the [O III]/ $H\beta$ ratio in comparison with H II regions. Besides, Lac18 defines a criterion of DIG definition in function of the $H\alpha$ equivalent width ($EW(H\alpha)$), based on if the region is dominated by photoionisation by HOLMES, corresponding to a $EW(H\alpha) < 3 \text{ \AA}$ (hDIG). The hDIG would be then the main regime in E-S0 galaxies, due to the old stellar populations that conforms this galaxies.

On the other hand, IFS-studies based on the MUSE instrument (Multi Unit Spectroscopic Explorer; Bacon et al. 2010) or wide field spectroscopic coverage such as TYPHOON (Grasha 2022) offer datasets with a spatial resolution ranging from ~ 50 pc to the resolution of MaNGA-like galaxies, that allows for a spatially resolved study of the DIG and H II regions. Nevertheless, the studies of the DIG using resolutions of ~ 50 pc have predominantly focused on the best galaxies within these surveys in terms of spatial resolution. These studies typically involve individual galaxies, such as M83 (Poetrodjojo et al. 2019; Della Bruna et al. 2022a,b), or the 19 galaxies encompassed by the PHANGS project (Physics at High Angular resolution in Nearby Galaxies; Emsellem et al. 2022; Belfiore et al. 2022, hereafter Bel22), capable to resolve the ISM structure at ~ 50 pc of resolution. Studies conducted within the PHANGS galaxies reveals that photoionisation by HOLMES is more prevalent in central regions where $EW(H\alpha) < 3 \text{ \AA}$. In these regions, approximately 2% of the total $H\alpha$ emission is powered by HOLMES. The remaining emission arises from photon leakage from H II regions. The mean free path of ionised photons is estimated to be < 1.9 kpc, based on a straightforward thin-slab model for photon propagation through the ISM (Zurita et al. 2002; Seon 2009). This model also predicts an increase in the [O III]/ $H\beta$ ratio and the ionisation parameter, which contradicts the decrease in the ratio as $\Sigma_{H\alpha}$ increases. However, the contribution of the spectral hardness of HOLMES to the ionisation budget explains this discrepancy and the trend of increasing [S II]/ $H\alpha$, [N II]/ $H\alpha$, and [O I]/ $H\alpha$ line ratios as $\Sigma_{H\alpha}$ decreases.

In order to make progress in quantifying the escape fraction of ionising photons from H II regions, it is imperative to reassess the importance of leaked radiation and HOLMES in contributing to the ionisation of the DIG in star-forming disk galaxies. However, previous studies aimed at this task have relied on large surveys with low spatial resolution or small samples with high spatial resolution. In most cases, these studies have employed

methodologies that primarily rely on $H\alpha$ emissions for the definition and exploration of the DIG.

In this paper, we introduce the Bidimensional Exploration of the warm-Temperature Ionised gaS (BETIS) project. The main goals of BETIS are the exploration of potential ionisation mechanisms, assessment of the DIG's influence on calculating chemical abundances and star formation rates, and examination of the correlations between the DIG and various factors such as galaxy morphology, star formation rate, neutral hydrogen abundance, and other physical parameters.

This paper is structured as follows: Sec. 2, provides a definition of the sample selection from different MUSE observations. Sec. 3 outlines the methodology for distinguishing between DIG emission and H II regions emission. We also introduce a novel adaptive binning method that will be applied at the observed data-cubes, designed to enhance the signal-to-noise ratio of our data. This methodology is tested on a showcase subsample presented in Sec. 4, showing preliminary results, as well as a discussion of the challenges encountered when using $EW(H\alpha)$ as a proxy for characterising the DIG. Finally, the Sec. 5 provides an overview of the key findings and outcomes presented in this paper. Additionally, we outline our plans for future research, specifically focusing on the forthcoming parts of the DIG analysis with the rest of the BETIS sample.

The following notation is used throughout the paper: $[N II] \equiv [N II] \lambda 6584$; $[S II] \equiv [S II] \lambda 6717 + [S II] \lambda 6731$; $[O III] \equiv [O III] \lambda 5007$; and $[O I] \equiv [O I] \lambda 6300$. We adopt the standard Λ CDM cosmology with $H_0 = 70$ km/s/Mpc, $\Omega_\Lambda = 0.7$, $\Omega_M = 0.3$.

2. The BETIS sample

The task of characterising and understanding the DIG in star-forming requires spatially resolved information, in order to discern the DIG emission from the H II regions and explore the possible ionisation mechanisms. For this reason, the IFS surveys are the ideal data sets for study the DIG, for instance, MaNGA (Z17) and CALIFA (Lac18), since they bring the necessary optical coverage to undertake this challenge. However, the limited spatial resolution has been the main obstacle of these studies. In terms of resolution and spectral coverage, MUSE is one of the best instruments to study the DIG at extragalactic level.

MUSE is an IFS located at the ESO-VLT 8.1m telescope at Cerro Paranal, Chile. The instrument brings 1 arcmin² of field of view (FoV), with a sampling of 0.2×0.2 arcsec, a spectral range of 4650 – 9300 Å, with a resolution of 1750 at 4650 Å to 3750 at 9300 Å, and a spectral sampling of 1.25 Å. The data observed by this instrument has already been used to study the DIG (PHANGS-MUSE; Bel22; Della Bruna et al. 2022a,b; Congiu et al. 2023) at a spatial resolution of ~ 50 pc, but constrained to only < 20 objects.

In order to perform an exhaustive, reliable and statistical significant analysis of the DIG, the sample needs to cover a broad range of star-forming galaxies across all morphological types, as well as a suitable spatial resolution to discern the DIG emission from H II regions ($\lesssim 0.5$ kpc). For this reason, the BETIS sample was selected from observational projects of local galaxies that meet the previous conditions.

The first of these projects is AMUSING (The All-weather MUSE Supernova Integral-field of Nearby Galaxies; Galbany et al. 2016). This survey is an ongoing project aimed at studying the environments of supernovae by means of the analysis of a large number of nearby supernova host galaxies ($0.005 <$

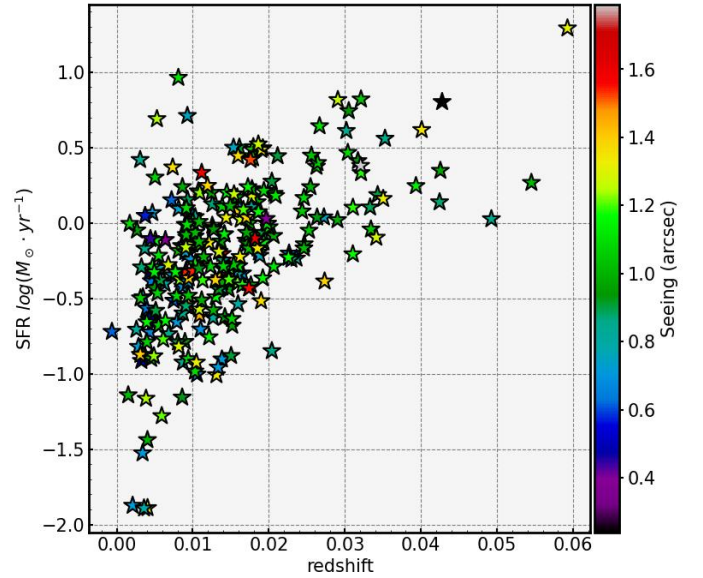


Fig. 1. Distribution of star formation rate versus redshift of the BETIS sample. The colorbar represent the seeing reported in every cube, with a median of ~ 1 arcsec.

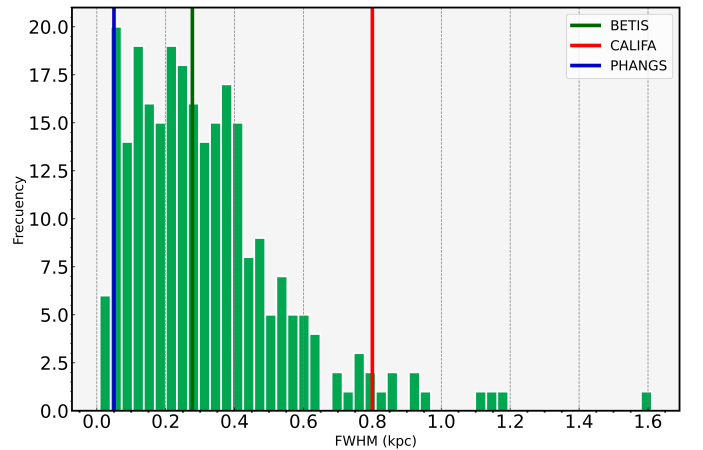


Fig. 2. PSF spatial resolution (FWHM, in kpc) of the BETIS sample. The three vertical lines represents the mean FWHM of three samples: ~ 0.8 kpc for Lac18, ~ 275 pc for BETIS and ~ 50 pc for Bel22.

$z < 0.1$). The AMUSING survey¹ currently comprises 571 supernova hosts observed during the semesters P95-P104 (April 2015-March 2020) and is composed by a wide variety of galaxy types with the common characteristic of having hosted a known supernova.

Alongside the AMUSING survey, several new objects have been observed with MUSE in different programmes; the AMUSING+ sample (Galbany et al. in prep.) aimed to increase the number of supernova hosts, and AMUSING++ (López-Cobá et al. 2020), a compilation of MUSE observations with the goal of investigating the presence of galactic outflows. The AMUSING++ compilation includes galaxies from different MUSE projects:

- CALIFA galaxies observed with MUSE in the ESO archive.
- The GAs Stripping Phenomena in galaxies with MUSE (GASP; Poggianti et al. 2017).

¹ The AMUSING survey characterisation is available online: <https://amusing-muse.github.io/sample/>

Galaxy	Type	RA	DEC	d (kpc)	redshift	seeing (")	FWHM (pc)	Incl (°)	PA (°)	pc/spx	Survey
NGC863	SA(s)a	02h14m	-00d46m	34	0.02639	1.08	591.98	22.40	175.6	109	AM+
NGC3393	(R')SB(rs)a	10h48m	-25d09m	69	0.01246	0.98	253.56	25.74	12.8	51	AM+
NGC6627	(R')SB(s)b	18h22m	15d41m	28	0.01771	0.81	297.82	25.12	70.0	73	AM
NGC692	(R')SB(r)bc	01h48m	-48d38m	96	0.02115	0.90	395.21	30.30	84.4	87	AM
ESO584-7	Sc	16h12m	-21d37m	65	0.03171	0.94	618.88	45.12	148.0	131	AM
ESO325-43	SAB(s)c pec	13h59m	-37d51m	107	0.03503	1.32	960.03	38.37	115.0	145	AM
IC3476	IB(s)m	12h32m	14d03m	10	-0.00063	0.62	49.60	33.99	30.0	16	AM+

Table 1. General characteristics of the BETIS sample, in order of morphological type. The columns represents, from left to right: The designation of the galaxy, the morphological Hubble-De Vaculeurs type, the RA and DEC in the J2000 epoch of the center of the galaxies, restricted from the Paranal observatory ($DEC < 25^\circ$), the physical diameter (d) in kpc, the redshift, the measured seeing in arcsecs (as the 'TEL.IA.FWHMOBS' parameter in the header of the .fits files from the datacubes), the PSF FWHM in pc, inclination with respect to the line of sight, the position angle (in deg) and the physical size of the spaxel, in parsec/spaxel. The last column is the program where the object is drawn (AM(+/-)): AMUSING(+/-). The RA, DEC, the diameter and the redshift are obtained from NED. The morphological type and position angle, from Hyperleda. The full table is available in the online version of this article.

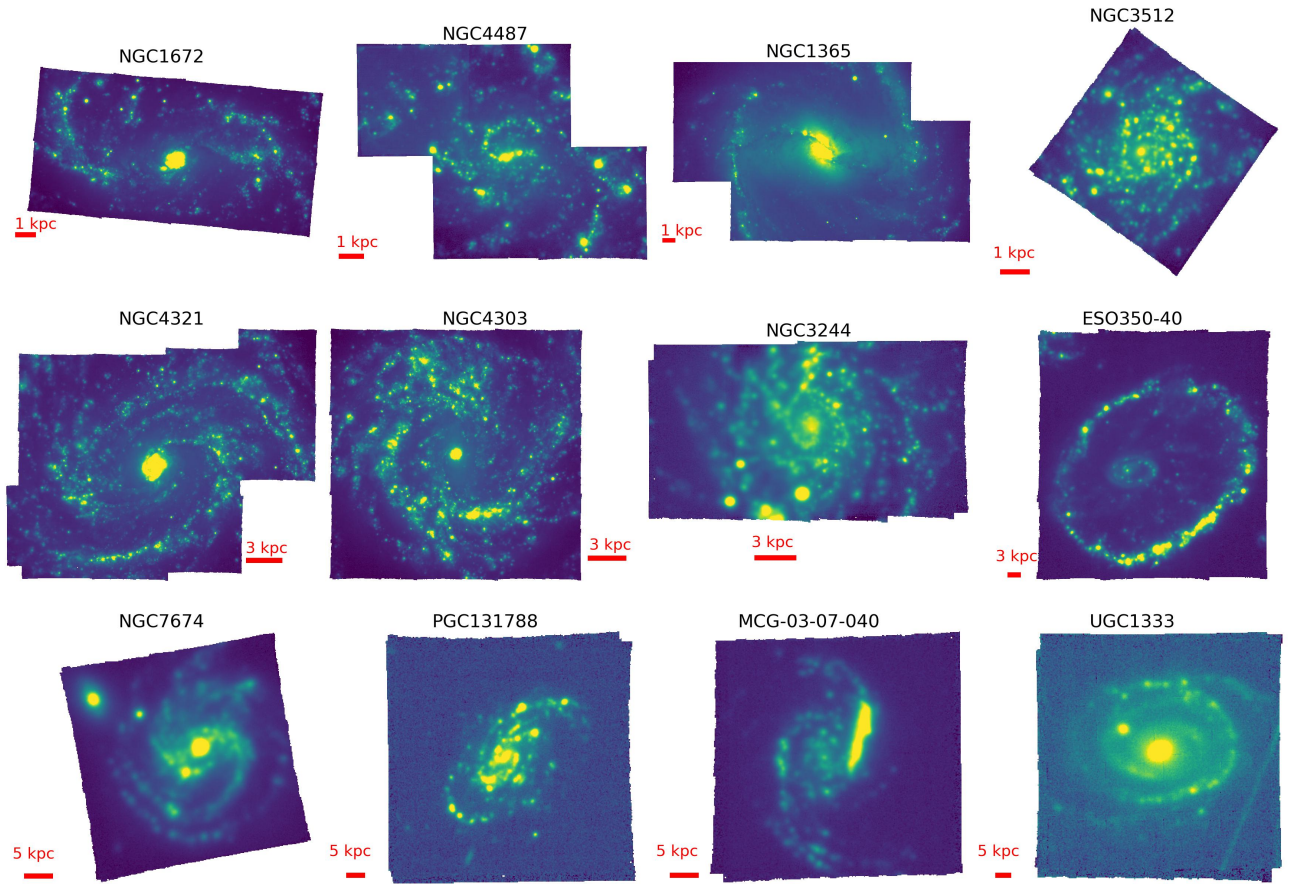


Fig. 3. $H\alpha$ images from the BETIS galaxies. The four on the top are PHANGS-type galaxies, with FWHM = 25.19, 52.23, 65.35 and 85.58 pc respectively. The four on the middle are BETIS-type, with FWHM = 111.99, 136.23, 256.64 and 527.95 pc respectively. The four on the bottom are CALIFA-like galaxies, with FWHM = 760.39, 859.05, 1191.7, 1611.46 pc respectively. The first and the last galaxy of this figure are the best and the worst galaxy of the BETIS sample in terms of spatial resolution.

- The MUSE Atlas of Disks (MAD; [Erroz-Ferrer et al. 2019](#)).
- The Time Inference with MUSE in Extragalactic Rings (TIMER; [Gadotti et al. 2019](#)).
- The Close AGN Reference Survey (CARS; [Husemann et al. 2019](#)).

AMUSING+ adds 143 objects to the previous AMUSING sample, while AMUSING++ adds up 410 objects, making a total of 1124 objects. We will refer to this sample of 1124 nearby objects observed with MUSE-VLT as the AMUSING(+++) sample. The datacubes have been reduced using the ESO reduction pipeline², more information about the data and data reduction of each project can be found in the corresponding paper. The datacubes are available in the ESO Science Archive Facility.³

The main bottleneck for performing a reliable DIG analysis is the spatial resolution. We need enough resolution to sample the DIG with respect the size, inclination and morphology of star-forming galaxies, and being able to distinguishing the H II regions emission from DIG emission. For this reason, we perform an exhaustive visual inspection of the 1124 AMUSING(+++) datacubes using $H\alpha$ images, obtained summing 10 frames of the datacubes centered in $H\alpha$ with a 12.5 Å width. We exclude those galaxies whose resolution or angular size with respect the FoV are not optimal for the spatially resolved study of the DIG, and object with low data quality. This criteria leaves us with 265 galaxies optimal for BETIS. Table 1 shows general information of part of the sample (full table is available online).

The BETIS sample is composed by nearby galaxies, between 6.5 and 253.7 Mpc of distance, and redshifts⁴ between $0.00 < z < 0.06$, with a mean value of 0.015 and a median of 0.013. The masses spans between $10^8 M_\odot$ and $10^{12} M_\odot$ (López-Cobá et al. 2020), with a mean value of $\sim 10^{11} M_\odot$, and the star formation rate (SFR⁵) between 0.01 and 19.5 M_\odot/yr , with a mean value of 1.1 M_\odot/yr . The sample includes 9 galaxies with low rate of star formation (< 0.1) and one galaxy (UGC1333) considered a starburst galaxy, with a $\text{SFR} > 10 M_\odot/\text{yr}$ (see Fig. 1). Thus, most of the sample lies within ranges of typical spiral galaxies SFRs and fits the distribution of masses and SFRs at $z \sim 0$ in the star formation main sequence (SFMS, Boquien et al. 2014; Sparre et al. 2015).

Fig. 2 shows the spatial resolution of the BETIS sample. The resolution is limited by seeing, the physical scale of the galaxies is linked to the PSF FWHM, measured as the seeing. The median seeing is ~ 1.02 arcsec (0.24 standard deviation, Fig. 1), this corresponds to mean physical resolution of ~ 275 pc (green line). The 96% of the sample has better resolution than the mean CALIFA FWHM (red line), while the 23% has better resolution than the CALIFA galaxy with the highest resolution (200 pc of FWHM). The BETIS sample includes 10 objects with a spatial resolution comparable with that of the PHANGS sample (blue line, < 50 pc). The combination of spatial resolution and number statistics is a clear advantage of the BETIS data set for the study of the DIG. See Fig. 3 for a general overview of the sample resolution.

The BETIS sample has a broad distribution of sizes and inclinations. Around 25% of the galaxies have $r_{25,B} < 42''$, meaning that the entire galaxy fits inside the MUSE FoV, 58 galaxies are mosaics that consist in various pointings of the telescope, and these objects represents the galaxies with the best spatial resolution of the sample. The inclinations span between face-on and edge-on galaxies, being the 37% of the galaxies (99 galaxies) inclined less than 45° with respect the line of sight, and 14% of

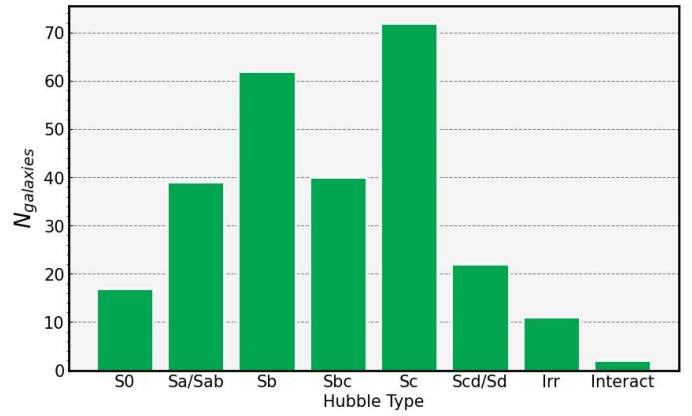


Fig. 4. Hubble morphological type distribution of the BETIS sample, from the Hyperlede database (Makarov et al. 2014).

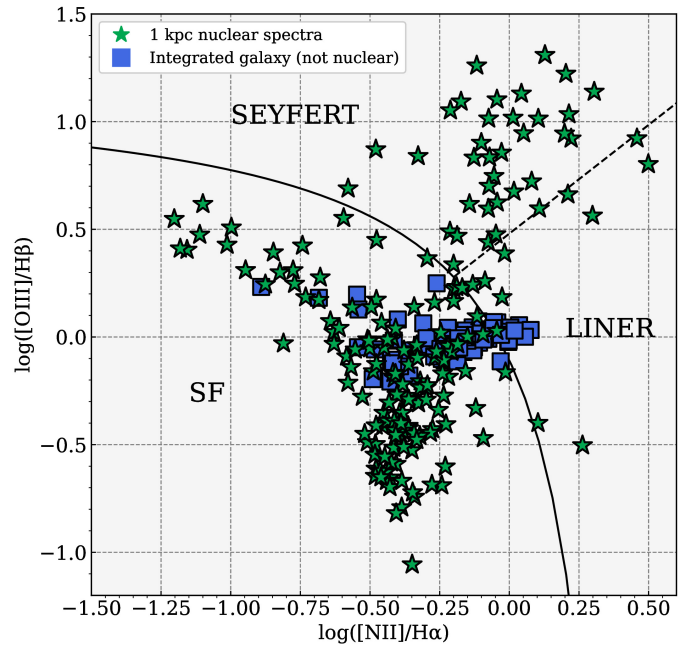


Fig. 5. BPT diagram for the BETIS sample. The integrated spectra of a 1 kpc aperture centred in the nucleus of 186 galaxies are represented by the green stars. Meanwhile, the blue squares represent the integrated spectra of the galaxies whose nucleus is not included in the datacube. Solid line demarcation between star-forming and AGN regimes is given by Kewley et al. (2001). Dashed line demarcation between Seyfert and LINER regimes is given by Cid Fernandes et al. (2010).

them (37 galaxies) inclined more than 75° , with an average inclination of 52° for all the sample.

Fig. 4 shows the morphological distribution of the 265 galaxies that compose the BETIS sample. The distribution is the following: 17 lenticular (S0) galaxies, 35 Sa, 4 Sab, 62 Sb, 40 Sbc, 72 Sc, 5 Scd, 17 Sd, and 11 irregular galaxies. For convenience, we aggregate the sample in 7 main types; S0 (6.5% of the total), Sa/Sab (15%), Sb (23.6%), Sbc (15.2%), Sc (27.3%), Scd/Sd (8.4%) and irregulars (4%), so we can infer general properties of the DIG in function of the morphology. We included in the BETIS sample two system of galaxies in interaction; the pair ARP144, and the ring shaped galaxy ESO350-40 (The Cartwheel) in order to study the DIG behaviour in galaxies where matter injections occurs and where the disk of the galaxy is deformed.

² <http://www.eso.org/sci/software/pipelines/>.

³ ESO Science Archive Facility: <http://archive.eso.org/cms.html>

⁴ All redshift values correspond to the heliocentric redshift, obtained from the NED database: <http://ned.ipac.caltech.edu/>.

⁵ Obtained as $\text{SFR} = L(\text{H}\alpha) / 7 \cdot 10^{40} \text{ erg/s}$, using the $H\alpha$ images previously mentioned.

Fig. 5 shows a BPT diagram (Baldwin et al. 1981) for the nuclear emission of 186 of the galaxies of the sample, obtained by integrating spectra of a region of 1 kpc around the center of the galaxies whose nucleus is in the FoV of the observation (for the fluxes measurement see Sec. 3.2). For the remaining galaxies we integrated the entire FoV. The BETIS sample includes 21 LINER and 35 Seyfert galaxies.

3. Methodology

The study of extragalactic DIG has conventionally relied on analyses of high resolution narrowband $H\alpha$ and images of nearby galaxies ($z < 0.01$, Rand et al. 1990; Dettmar 1990; Ferguson et al. 1996a; Zurita et al. 2000), or long-slit spectroscopy with limited spatial coverage (Reynolds 1985; Wang et al. 1997; Otte et al. 2001; Hoopes & Walterbos 2003; Haffner et al. 2009a). In these studies, the methodology for subtracting the DIG from the galaxies and distinguish their emission from the H II regions emission is typically made using cut-offs in the surface brightness ($\Sigma_{H\alpha}$) of the $H\alpha$ line, and in those studies with images with high resolution, a morphological definition of the H II regions using automatised tools was performed (Walterbos & Braun 1994; Zurita et al. 2000, 2002; Oey et al. 2007). Nevertheless, these studies were constrained only to less than 5 face-on and edge-on galaxies in their sample, based only in $H\alpha$ in those studies with high resolution, and with low resolution in those with spectroscopic information. However, the use of the IFS in recent years allows to perform methodologies of DIG subtraction and analysis based on spatially-resolved spectroscopic information with broad samples, (e.g. MaNGA, CALIFA or PHANGS).

For example, the DIG studies using data from the MaNGA survey (Z17, Jones et al. 2017) made use of 365 nearly face-on star-forming galaxies with 2.5 arcsec PSF FWHM, which is not enough to resolve individual H II regions which typical sizes are ~ 100 pc. In this particular case, Z17 performed a cut out on $\Sigma_{H\alpha} > 10^{39} \text{ erg} \cdot \text{s}^{-1} \cdot \text{kpc}^{-2}$ to select those spaxels dominated by H II regions emission. On the other hand, the studies based on CALIFA data (Lac18), made use of 391 galaxies with a median PSF FWHM of ~ 0.8 kpc and proposed an alternative method to separate the DIG and the H II regions using the $H\alpha$ equivalent width ($EW(H\alpha)$), since —according to the authors— this parameter is a more appropriate proxy to distinguish the fundamental differences between the DIG and the star forming regions in comparison with the $\Sigma_{H\alpha}$. In addition, the authors argue that the usage of $\Sigma_{H\alpha}$ could led to misclassify low surface brightness H II regions as DIG.

Other authors have used the criteria to define and classify the DIG regime based on $EW(H\alpha)$ continued to be used to define the DIG (Vale Asari et al. 2019; Espinosa-Ponce et al. 2020). However, redefining the DIG a priori as the ionised gas consistent with ionisation from HOLMES could be problematic if the main goal is to discern the different ionisation mechanisms (Bel22). This is a challenging problem, as the standard resolution of CALIFA or MaNGA can not discern individual H II regions in order to characterise the DIG morphologically. In addition, the high spatial resolution of some galaxies observed by IFS (e.g. M83-TYPHOON/PrISM; Poetrodjojo et al. 2019, M83-MUSE; Della Bruna et al. 2022a, PHANGS-MUSE; (Bel22, Congiu et al. 2023)), enables the use automated tools in order to detect and remove individual H II regions in IFU datacubes with resolutions ~ 50 pc, but constrained to a few objects.

In our work, we outline the approach for determining the DIG by utilising the spectroscopic and morphological data generated by the MUSE-IFS, using a broad dataset with high res-

olution and with spectroscopic information, not only $H\alpha$. Our sample of 265 MUSE galaxies varies in morphology, properties and inclination, with resolutions enabling us to define the DIG and H II regions morphologically. A summary of the methodology, designed for galaxies of inclinations below 45° , is provided below, and it is subsequently explained in further detail in the following subsections:

- (i) In order to increase the signal-to-noise (SN) of the weak, low-surface brightness emission lines involved in the DIG study, a modified version of the adaptive binning technique of Li et al. (2023) is performed to the SN map of the [S II] line, obtaining then a segmentation map of the galaxy. The segmentation map is then applied to the datacube, in order to getting a binned datacube, in which each bin corresponds to the integrated spectra as the sum of the spaxels contained in the bin.
- (ii) Spectral fitting is performed on the binned spectra in order to derive emission line maps of the most important species for the DIG study. We consider 9 species, the hydrogen $H\alpha$ and $H\beta$ Balmer recombination lines, the He I $\lambda 5876$ recombination line, and the collisionally excited forbidden lines: [O III] $\lambda 5007$, [O I] $\lambda 6300$ and the doublets [N II] $\lambda 6548, 6584$ and [S II] $\lambda 6717, 6731$. The $H\alpha$ and $H\beta$ equivalent widths are also calculated during this step.
- (iii) The DIG is separated from the emission of the H II regions using a combination of an automated tool to detect and subtract the H II regions from the binned $H\alpha$ maps, and a cut-off in $H\alpha$ surface brightness ($\Sigma_{H\alpha}$) to subtract bright, irregular H II regions not detected by the automated tools. This results in a mask that corresponds to the lower-limit of the DIG. This mask is applied to all the binned emission line maps, creating a set of the lower-limit DIG emission. The upper-limit DIG emission is derived from the lower-limit binned maps considering a constant DIG emission column above the projected areas of the H II regions.

We will generalise the methodology for inclinations above 45° and edge-on galaxies in future papers.

3.1. Adaptive binning

Typically, the distinction between SF regions and DIG has been made using $H\alpha$, but if we aim to explore the DIG in using all available spectroscopic information, we must consider key emission lines in the study of the DIG, such as [O I], [N II], [O III] and [S II]. For a reliable analysis of the DIG, is crucial to take into account SN limitations of the data, specially in those lines of lower surface brightness, such as those mentioned above.

The signal of an emission line feature of a spectrum can be defined as the difference between the maximum flux value of an emission line $f(\lambda_{em})$ centred on λ_{em} of width w_{em} (in Å), and the mean of the fluxes in the two adjacent pseudo-continuum bands $f(\lambda_{c1})$ and $f(\lambda_{c2})$ of width w_{c1} , w_{c2} , measured on the spectrum of a given spaxel; and the noise corresponds to the mean of the flux within the two adjacent pseudo-continuum bands $f(\lambda_{c1})$ and $f(\lambda_{c2})$ (Rosales-Ortega et al. 2012).

For the sake of clarity, in this work the SN of an emission line is the ratio of the amplitude of the emission line, defined as the peak of the line minus the mean flux of the pseudo-continuum, over the standard deviation of the adjacent pseudo-continuum on the spectrum:

$$SN(\lambda_{em}) = \frac{\mu}{\sigma} = \frac{f(\lambda_{em}) - \langle f(\lambda_{c1}), f(\lambda_{c2}) \rangle}{\sqrt{\sigma^2(f(\lambda_{c1}), f(\lambda_{c2}))}} \quad (1)$$

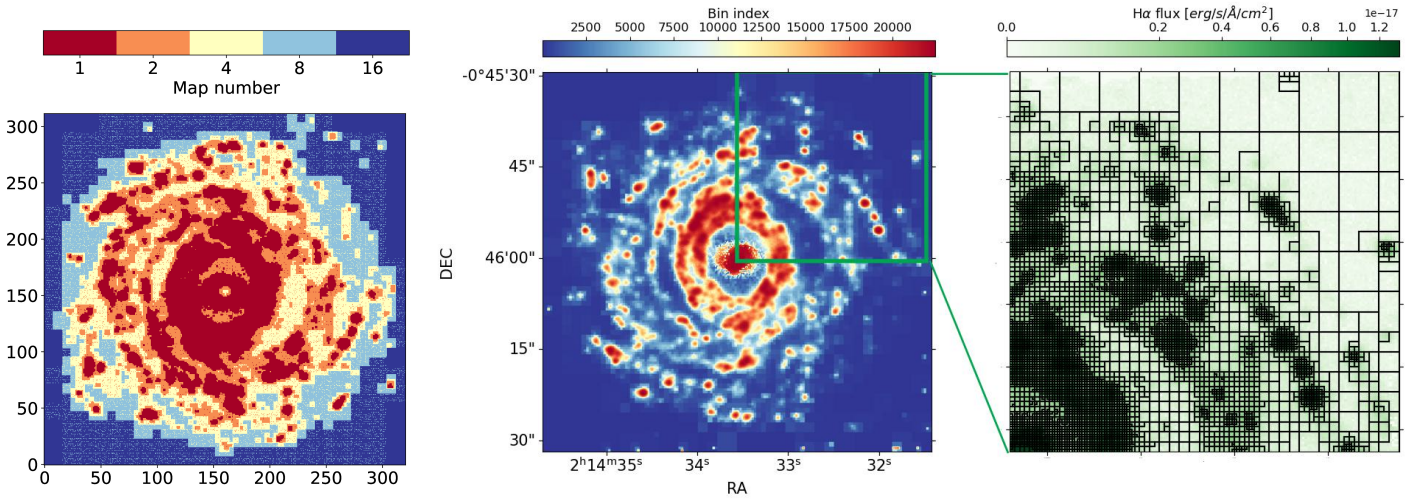


Fig. 6. Example of an adaptive binning of NGC 863 using $SN([S II]) = 10$ as target. The first figure represent the map numbers (map_N) from Li et al. (2023) algorithm. The second figure is the segmentation map obtained from our algorithm, where the bin index goes from $k = 1$ to N_{bins} . The third figure is a close-up of the segmentation map plotting the borders of the bins over the H α map. It is noticeable that the H II regions, whose SN is higher, are not binned, maintaining the structure pixel by pixel, and the bins are getting bigger as we move out of the H II regions.

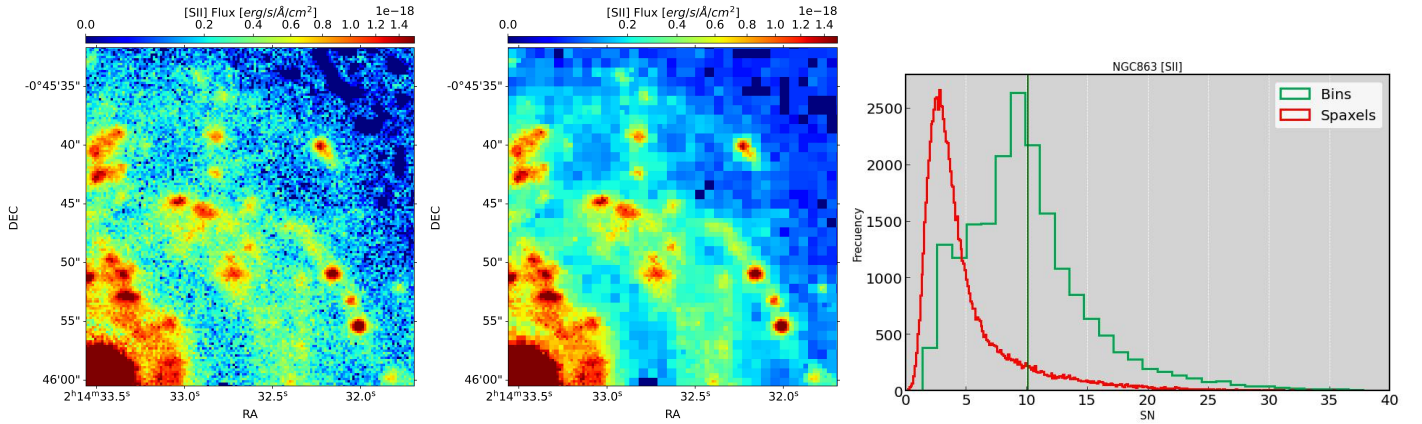


Fig. 7. NGC863. Left panel: [S II] emission line map obtained from the Gaussian fitting of the [S II] line from the nebular gas cube spaxel by spaxel. The nebular cube was obtained as the difference between the observed cube and stellar cube as described in Appendix A. Central panel: Binned [S II] emission line map, from the binned nebular gas cube, after performing an adaptive binning with target $SN([S II]) = 10$ to the observed cube, as described. Both panels are close-up of the same region than Fig. 6. Right panel: Distributions of SN ratio of [S II] line for NGC863, calculated with the equation 1. Red distribution corresponds to the $SN([S II])$ measured in the observed cube, i.e., the $SN([S II])$ of the spaxels. Green distribution corresponds to the $SN([S II])$ measured in the binned cube, i.e., the $SN([S II])$ of the bins. The vertical dark green line marks the mean value of the $SN([S II])$ of the bins, showing that the adaptive binning technique fulfils the goal of reaching a target $SN([S II]) = 10$ on average.

The most commonly employed approach to enhance the SN ratio of the data is to conduct adaptive binning, where individual pixels are combined into larger entities known as "bins" until the desired target SN is achieved. However, this comes at the expense of diminished spatial resolution. The Voronoi binning method (Okabe et al. 2000; Cappellari & Copin 2003) generally resolves the issue of retaining the highest spatial resolution of the images while adhering to the minimum SN limitation. This is achieved by tessellating the image and adjusting the bin size to ensure that every bin attains the desired SN. However, this technique is particularly well-suited for analyzing elliptical and featureless galaxies as it relies on the continuum SN ratio. It may not be as effective for our purpose, as our maps show irregular structures, like those depicting nebular gas emission lines. Consequently, we require an alternative method to avoid losing the primary morphology of spiral galaxies.

To solve this, we use a modified version of the adaptive binning method introduced by Li et al. (2023) in order to enhance the SN of weak emission lines. The code takes the flux of the line, the noise and a target SN as input, it creates a series of maps which cover the same area as the input data ($map_1, \dots, map_N, \dots, map_{N_{max}}$), as seen in Fig. 6. For each map_N the set of $N \times N$ pixels will be averaged, and, in consequence, the SN will be increased. If the SN of the bin is not the target SN, the code takes map_{N+1} instead. In our algorithm, we modify this code in order to get a segmentation map for binning the observed cube and getting a set of binned emission line maps, one per considered line. The new binning technique is carried out as follows:

1. We take as input the signal and noise defined in Eq. 1 and a target SN. The code will create the series of map_N , however, instead of recover the new averaged flux, we save an index k in the coordinates $[i_0, j_0], [i_0, j_1], [i_1, j_0], [i_1, j_1], \dots, [i_N, j_N]$

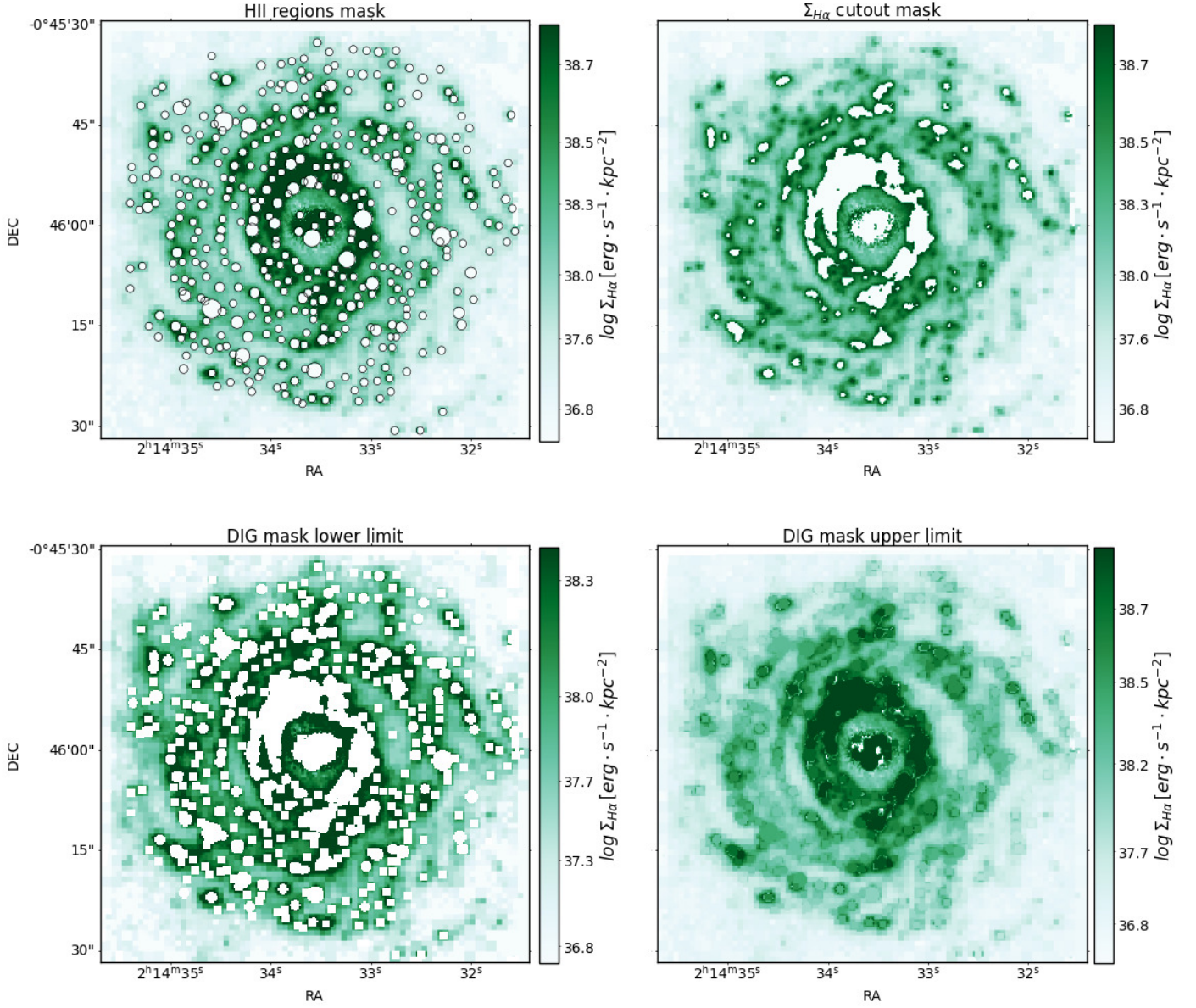


Fig. 8. Steps to get the lower and upper DIG limit for NGC 863 galaxy. The upper-left figure corresponds to the DIG mask obtained by masking the H II candidates given by the centroids and radii obtained from `pyHIIEXTRACTOR` to the binned $H\alpha$ map. The upper-right figure corresponds to the binned $H\alpha$ map after applying a $3\sigma_{\Sigma(H\alpha)}$ cut-off. The lower-left figure is the mask of the lower limit of the DIG, obtained as the combination of the upper-left and upper-right masks. The lower-right corresponds to the upper limit, assuming a constant non-zero flux level above the H II regions, interpolating the flux around these regions.

- whose flux would be averaged. The next subset of coordinates whose flux will be averaged will have an index $k+1$.
2. We perform the previous step for all subsets of coordinates for $k = 1, \dots, N_{bins}$ will result in a segmentation map, with the lowest bin indices k corresponding to the higher bins, i.e., the 1×1 bins that correspond to the pixels with SN higher than the SN target, and the lower indices corresponding to the bigger bins, i.e., those who needs more pixels to reach the target SN, as seen in Fig. 6.
 3. For each bin of the segmentation map, we save the integrated spectra of the observed cube as the sum of the spaxels contained in the bin. This result in a binned observed datacube.

Binning the observed cube offers the advantage of enhancing the SN of the spectra, rather than merely reducing the relative error associated to the Gaussian fitting of the lines, as is the case with direct binning the emission line maps. Moreover, if

our goal includes generating binned EW maps, it is not methodologically correct to bin the EW map obtained through spaxel-by-spaxel fitting. This is because EW is not an additive quantity; it varies when there are changes in the underlying stellar continuum. Hence, it is important to calculate the new EW from the integrated spectra. If we want to increase the SN of all the lines of interest, we need to choose a target feature as a basis to construct the segmentation map for the observed cube, ensuring to recover the maximum spatial information and signal in the DIG regimes. We employ $\text{SN}([S II])$ as the target for adaptive binning because it is a low-ionisation collisional excitation line that remains unaffected by the correction for stellar population after the spectral fitting process.

Considering the most important low-ionisation species that are found enhanced in the DIG regimes in SF galaxies, such as $[N II]$ and $[S II]$ (Z17; Lac18), the $[S II]$ line exhibits the lowest

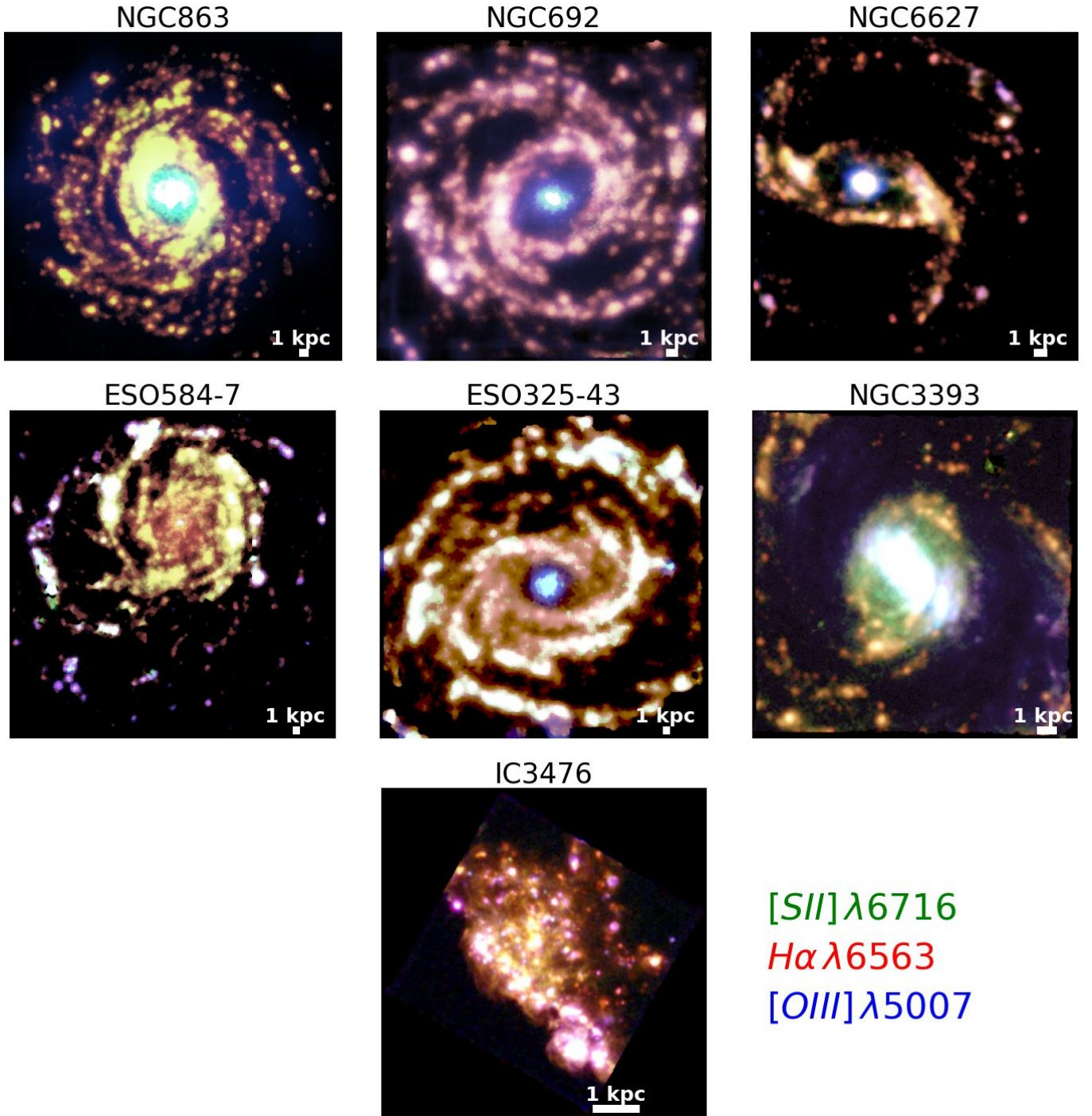


Fig. 9. RGB synthetic images of the galaxies selected for our subsample. The images are constructed as a composition of the $[S II] \lambda 6716$ (green), $H\alpha$ (red) and $[O III] \lambda 5007$ (blue) spaxel by spaxel emission maps obtained following the methodology explained in section 3.2.

SN (mean of 5, median of 3) among the low ionisation species. Furthermore, the $[O III]$ line exhibits a mean SN of 2.5, therefore, if a $\sim 5\sigma$ detection is required, the SN needs to be increased a factor of 7 (Bel22). To achieve this, we perform our adaptive binning method using $SN([S II]) = 10$ as target SN. Fig. 7 (right panel) shows the distribution of $SN([S II])$ obtained in the integrated spectra, where we can find that we get the average SN of 10 that we expected.

3.2. Spectral fitting

For every new spectrum we perform a SSP fitting with STARLIGHT (Cid Fernandes et al. 2005), getting nebula emission spectra as the difference between the integrated observed spectra and the synthetic stellar spectra obtained after the fitting. We use the CB07 base spectra for the fittings (Bruzual & Charlot 2003; Bruzual 2007b). The $N_* = 100$ SSPs from CB07 comprises 3 metallicities, $Z = 0.2 Z_\odot$, Z_\odot and $2.5 Z_\odot$, and 15 ages from $t = 0.001$ to $t = 13$ Gyr. All SSPs are normalized to $1M_\odot$ at $t = 0$. Their spectra were computed with Padova-2004 evolutionary tracks models, and Chabrier (2003) IMF ($0.1M_\odot < M <$

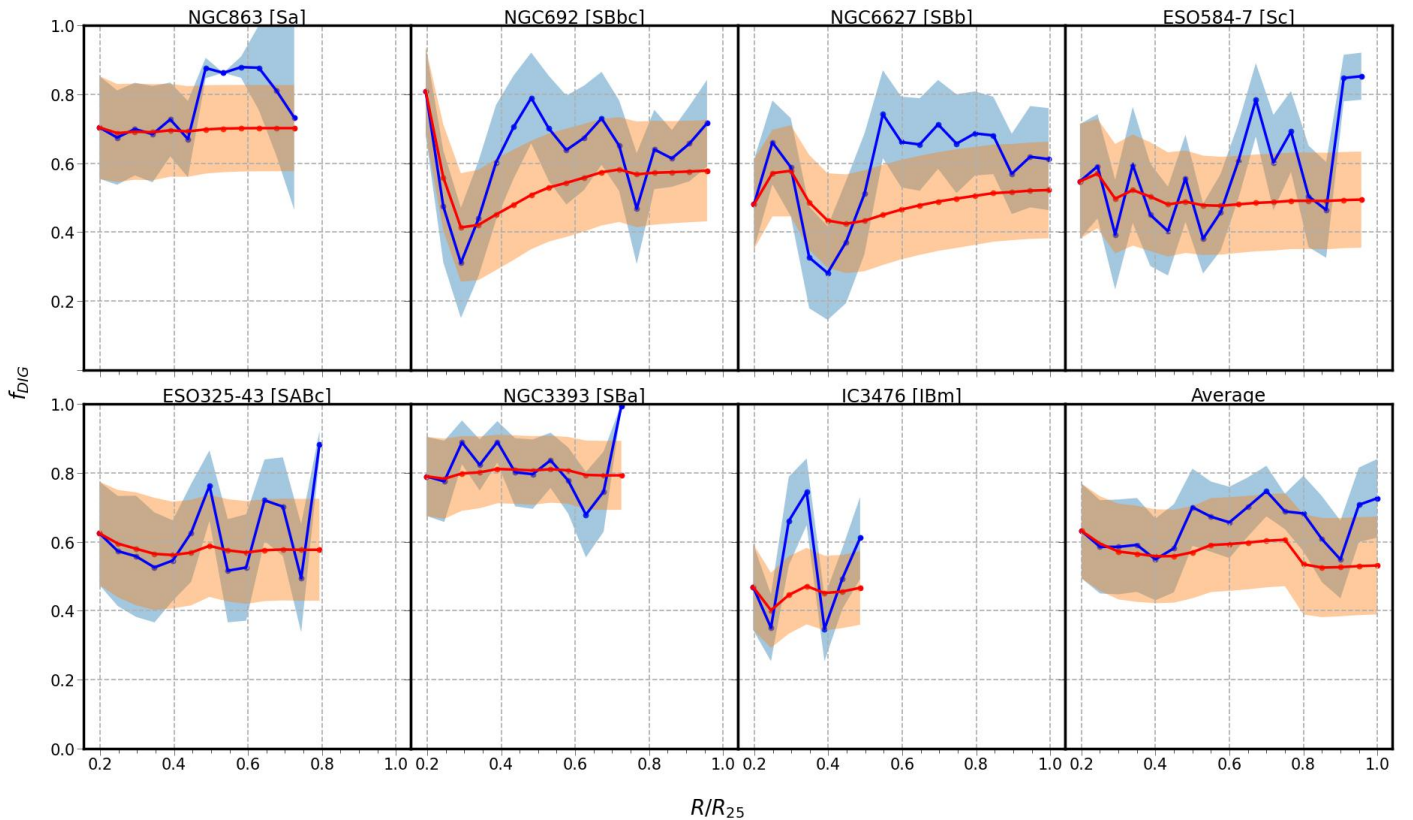


Fig. 10. Distribution of the DIG fraction ($f(\text{H}\alpha)_{\text{DIG}}/f(\text{H}\alpha)_{\text{total}}$) for each galaxy of the subsample. Red area represents the cumulative distribution between the the upper and lower DIG limits, with a step of $0.05R_{25}$, being the solid red lined the mean value. Blue area is the radial distribution of the DIG obtained integrating the flux between rings of width $0.05R_{25}$ and with a step of $0.05R_{25}$, being the solid blue lined the mean value. R_{25} is the isophote at the blue brightness of 25 mag/arcsec^2 . This parameter is obtained from hyperleda database.

100 M_{\odot}). Then we compute a Gaussian fitting around the 9 lines of interest previously mentioned on every nebular spectra, using the python library MPFIT, and resulting in a set of 9 binned emission line maps. See Appendix A for further details about the SSP fitting and emission line fits. Fig. 7 shows the difference between the [S II] emission line map obtained after performing the SSP fitting on the observed cube spaxel by spaxel (left panel) and on the binned cube applying the exposed method (center panel).

The $\text{H}\alpha$ and $\text{H}\beta$ equivalent width is also calculated during this step using the ratio between the integrated observed spectra and the fitted stellar model, resulting in a normalised stellar absorption spectra where the EW is fitted for every bin using again MPFIT.

3.3. Morphological definition of the DIG limits

The separation between SF regions and the DIG has been always the first topic of discussion when studying and analysing the physics of the DIG. Historically, the most common method has been to separate the DIG from SF regions based on a $\text{H}\alpha$ surface brightness ($\Sigma_{\text{H}\alpha}$) cut-off (Zurita et al. 2000; Oey et al. 2007; Z17). However, this method presents the problem of misclassifying low surface brightness H II regions as DIG, besides to the possibility of classifying the emission of two overlapped DIG regions as H II region (Lac18).

A suitable alternative for this problem is using automatised tools for the detection and subtraction of the H II regions individually. Several tools have been developed for this task, including SExtractor (Bertin & Arnouts 1996), HIIPHOT (Thilker et al. 2000), HIIPLOT (Sánchez et al. 2012), PYHIIPLOT

(Espinosa-Ponce et al. 2020), ASTRODENDRO (Della Bruna et al. 2022a) or PYHIIPLOT (Lugo-Aranda et al. 2022).

The spatial resolution is an important key to detect and define morphologically individual H II regions. For the specific range of resolutions of the BETIS sample, we use PYHIIPLOT (Lugo-Aranda et al. 2022) in order to detect H II regions candidates. The code detects the H II regions candidates and assigns them a radius and a centroid, in the image coordinates. It is highly efficient for the detection of circular H II regions, specially those with low $\Sigma_{\text{H}\alpha}$, solving the problem previously mentioned. Nevertheless, the limiting factor of this algorithms is in the complexity of the regions and in the variety of shapes and sizes of the brighter ones, hence a circular extraction is not sufficient for those complex regions, since it would not adapt to their morphology.

In the pursuit of the optimal methodology for segregating DIG emissions from H II regions, we conducted an extensive series of tests employing a variety of galaxies, techniques, and algorithms, considering the different observing conditions and depth of the BETIS sample. Our findings led us to the conclusion that, in order to establish a reliable morphological definition of the DIG, a combination of two methods is necessary:

- (i) The detection and masking of bona-fide H II regions exhibiting regular (circular) morphology based on the $\text{H}\alpha$ emission line map.
- (ii) The implementation of a cut-off in $\text{H}\alpha$ surface brightness to account for irregular and highly luminous H II regions that may elude automated masking tools.

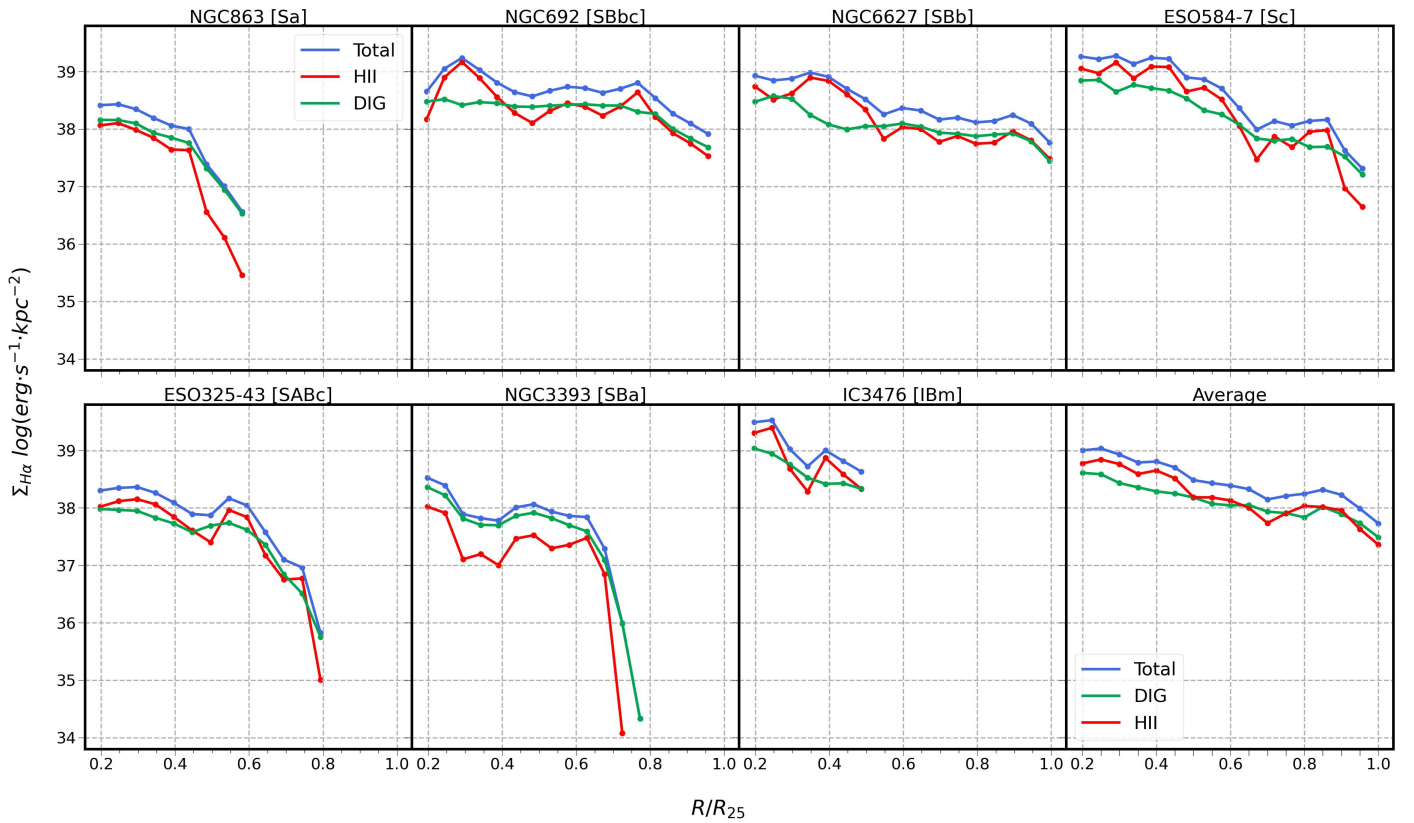


Fig. 11. Radial distribution of $\Sigma_{H\alpha}$ for each galaxy, obtained by measuring the surface brightness of a series of deprojected annulus centered at the nucleus of each galaxy with a width of $0.05R_{25}$. The distributions are performed for the entire galaxy (blue), the lower DIG limit (green) and HII regions (red). The last panel represent the mean distributions for the subsample.

For the first step, we make use of the code `PYHIIEXTRACTOR` for a first detection of the HII regions. The algorithm takes a $H\alpha$ map and detects the positions and radii of all the candidates HII regions. We use those positions and radii to perform a mask of HII regions, to be applied to the binned $H\alpha$ map.

For the second step, we perform a $\Sigma_{H\alpha}$ cut-off to the binned map. This cut-off is defined as three times the standard deviation of the surface brightness distribution of the masked map, as defined in the initial step ($3\sigma_{\Sigma(H\alpha)}$).

Performing a this cut-off will result in a second DIG mask, that in combination with the first step DIG mask will give us the lower limit of DIG, as seen in Fig. 8, since we are assuming that all the emission coming from the HII positions is due to the star formation and the DIG contribution can be neglected.

We can also estimate an upper limit for the DIG, rejecting the previous assumption and considering a constant DIG emission column above the projected areas of the HII regions (Zurita et al. 2000; Congiu et al. 2023). This limit is estimated in two steps: firstly, on every HII region of centroid ('X','Y') and radius 'R' detected by `PYHIIEXTRACTOR`, we define an annulus centred in that detection, with inner radius equal to the radius obtained, and outer radius 1.4 times the inner radius. We fill the HII region with the mean surface brightness measured inside the annulus. After performing this "filling" with every HII region detection, part of the galaxy is still masked due to the $\Sigma_{H\alpha}$ cut-off. To estimate the DIG contribution in these remaining regions, we fill them with the mean value of surface brightness of the border of the region. This result in a upper limit $H\alpha$ DIG map as seen in Fig. 8. The lower limit DIG mask is then applied to the rest of the binned emission line and EW maps, that is the basis of our data.

4. BETIS: first results

4.1. Showcase subsample

In order to illustrate the methodology and present initial findings of this analysis, a representative subset of 7 galaxies of different morphologies, characteristics and resolutions has been selected from the entire BETIS sample. This showcase subsample has been carefully chosen to provide insight into the broader study and serves as a demonstration of the methodology employed. The showcase subsample is listed in Table 1. Fig. 9 shows false-colour images of the subsample constructed as a composition of the [S II] (green), $H\alpha$ (red) and [O III] (blue) emission line maps obtained following the methodology described in Sec. 3.2 but on spaxel-by-spaxel basis. The native spatial resolutions vary from 49 pc (IC3476, i.e. PHANGS-like) to 960 pc (ESO325-43, CALIFA-like), with a median resolution of 395 pc. The subsample includes 3 known AGNs: NGC863 and NGC3393 are Seyfert 2 (Weedman 1977; Lipovetsky et al. 1988), and NGC692 which is a Low-Luminosity AGN (LLAGN; Zaw et al. 2019). We deliberately incorporated these AGNs into our study to investigate their impact when examining the ionisation mechanisms of the (DIG) within a sample comprising galaxies exhibiting various types of activity.

After performing the binning methodology outlined previously, we find an average bin size of the subsample of 627 pc (see Table 2 for a overview of the increment of the SN after binning). The average bin size in our subsample is larger than the typical bin sizes in studies of narrowband $H\alpha$ images (e.g. ~ 250 pc, Ferguson et al. 1996a; ~ 35 pc (native), Zurita et al. 2000; ~ 475 pc, Oey et al. 2007). Moreover, the bins dimensions exceed those of the mean Voronoi bins of the PHANGS-MUSE

Line	H α	H β	[N II]	[S II]	[O I]	[O III]
% SN (spax)	65	27	50	41	11	51
% SN (bin)	96	90	93	91	63	82

Table 2. First column is the percentage of spaxels and bins of the subsample whose SN(H α) is higher than 3. The rest of the columns represent the percentage of the spaxels and bins with SN of H α and SN of the correspondent line higher than 3.

sample (~ 200 pc; Bel22). Nonetheless, they are smaller than the average PSF FWHM of the CALIFA galaxies (~ 800 pc; Lac18).

4.2. The DIG fraction

The visual inspection and variation of the DIG, both within individual galaxies and across them, provide valuable insights into its origins. In the binned H α maps of our showcase subsample galaxies, a diverse range of structures within the ionised gas regions becomes evident. The variations in H α emissions in different directions yield crucial information about the evenness on the intensity of the DIG distribution and its spatial association with prominent H II regions. Likewise, investigating changes in the diffuse fraction and H α surface distribution within a particular galaxy is of significant interest as it aids in pinpointing the source of the DIG.

Fig. 10 shows the distribution of the DIG fraction, defined as the ratio of the DIG flux to the total H α flux, $f(\text{H}\alpha)_{\text{DIG}}/f(\text{H}\alpha)_{\text{total}}$, for each galaxy of the subsample, in both radial and cumulative distributions. The radial distribution is obtained by measuring the DIG fraction from a series of deprojected rings centered at the nucleus of each galaxy with a width of $0.05R_{25}$, while the cumulative distribution is obtained by performing aperture photometry of the DIG fraction in the same series of deprojected rings that are used for deriving the radial profiles, for both the lower and upper DIG limits. Moreover, using the definition of radial distribution, we present in Fig. 11 the H α surface brightness distributions for the lower DIG limit (green) after applying the mask defined in Sec. 3.3, the galaxy with only H II regions (red) and the total galaxy (blue). All the fluxes from this section and hereafter have been corrected for interstellar extinction assuming the Cardelli extinction law, assuming $R_V = 3.1$ (Cardelli et al. 1989).

Overall, the radial distribution of the DIG fraction tends to increase, while the cumulative distributions remain constant, but is more affected by the galaxy morphology than the cumulative distribution. The presence of a barred structure in NGC692, NGC6627, and ESO325-43 is evident through a decline in both distributions between $0.2-0.4 R_{25}$, which decreases up to 20%. This effect is also reflected on the radial distributions of the H α surface brightness (Fig. 11), which show an increment of the $\Sigma_{\text{H}\alpha}$ for the H II regions distribution, reaching up to $10^{39} \text{ erg} \cdot \text{s}^{-1} \cdot \text{kpc}^{-2}$ between $0.2-0.4 R_{25}$ for those galaxies. NGC3393 exhibits the highest DIG fraction for both lower and upper limits (0.69-0.87), presenting a surface brightness that surpasses the H II regions, throughout the entire galaxy, resulting in a maximum difference of around 1 dex. Furthermore, NGC863 also exhibits higher $\Sigma_{\text{H}\alpha}$ in the DIG than in the H II regions, notably towards greater galactocentric radii.

The Sc galaxy ESO584-7 and the dwarf IBm galaxy IC3476 present the lower DIG fraction, 0.37-0.66 and 0.4-0.63 respectively. Additionally, they have the highest surface brightness for the H II regions in the subsample, being $>10^{39} \text{ erg} \cdot \text{s}^{-1} \cdot \text{kpc}^{-2}$ in the inner parts of the galaxy and decreasing to $\sim 5 \cdot 10^{38}$ at

$0.5R_{25}$. The average radial distribution of the DIG fraction is not showing any tendency in particular, remaining constant probably due to the mixture of morphologies of our showcase subsample. A full analysis considering a general distribution by morphological type will be carried out as part of BETIS in a forthcoming paper.

Table 3 summarises the results obtained from the DIG fraction for the showcase subsample. The general findings for this showcase subsample show that the DIG fraction ranges from 0.4 to 0.7, which coincides with the results of previous research, in both lower limit (e.g. Ferguson et al. 1996a,b; Zurita et al. 2000; Thilker et al. 2002; Oey et al. 2007; Bel22), and upper limit (e.g. Zurita et al. 2000; Congiu et al. 2023). Besides, the tendency of the cumulative distribution is to be constant and indicating approximately a 60% of DIG in these galaxies. The surface brightness of the DIG vary from $\sim 6 \cdot 10^{38}$ in the inner parts of the galaxies and decreasing monotonically to $\sim 5 \cdot 10^{37} \text{ erg} \cdot \text{s}^{-1} \cdot \text{kpc}^{-2}$ in the outer regions, with a notably high integrated H α luminosity between 10^{40} and $5 \cdot 10^{41} \text{ erg/s}$, which is consistent with previous studies (e.g. Ferguson et al. 1996a,b; Zurita et al. 2000).

The similarity in the $\Sigma_{\text{H}\alpha}$ radial distributions between the H II and DIG regimes and its impact in the DIG fraction supports the correlation between H II regions emission and DIG photoionisation (Ferguson et al. 1996a,b; Zurita et al. 2000). However, performing this exploration individually shows that there are instances where DIG $\Sigma_{\text{H}\alpha}$ values exceed those of the H II regions, in particular, in the two Seyfert galaxies, NGC863 and NGC3393. For instance, for NGC863, a total DIG $\Sigma_{\text{H}\alpha}$ of $6.6 \cdot 10^{38} \text{ erg} \cdot \text{s}^{-1} \cdot \text{kpc}^{-2}$ will require a power per unit area of $1.5 \cdot 10^{-3} \text{ erg} \cdot \text{s}^{-1} \cdot \text{cm}^{-2}$ to keep the DIG ionised, while the total $\Sigma_{\text{H}\alpha}$ of the H II regions of $5.02 \cdot 10^{38} \text{ erg} \cdot \text{s}^{-1} \cdot \text{kpc}^{-2}$ provides a power of $1.1 \cdot 10^{-3} \text{ erg} \cdot \text{s}^{-1} \cdot \text{cm}^{-2}$, which is insufficient to ionize the entire DIG⁶.

Hence, it is imperative to contemplate alternative ionisation sources that can provide additional energy supply to the ISM apart from Lyman continuum photons escaping from H II regions to keep the DIG ionised for those particular cases. The incorporation of collisional, low-excitation lines like [N II], [S II], or [O I], as well as high-excitation lines such as [O III] and He I in the analysis is essential for comprehensively investigating the diverse array of ionisation mechanisms that exist within the (ISM).

Galaxy	Type	$f_{\text{DIG,low}}$	$f_{\text{DIG,up}}$	$3\sigma_{\Sigma(\text{H}\alpha)}$	Bin size (pc)
NGC863	SA(s)a	0.45	0.75	38.8	743
NGC692	SBbc	0.44	0.73	39.1	578
NGC6627	SBb	0.39	0.67	39.3	490
ESO584-7	Sc	0.37	0.66	39.4	920
ESO325-43	SABc	0.44	0.75	38.5	1129
NGC3393	SBa	0.69	0.87	40.0	427
IC3476	IBm	0.40	0.63	39.8	101
Subsample	-	0.40	0.70	39.3	627

Table 3. Total DIG fraction for each galaxy. ' $f_{\text{DIG,low}}$ ' and ' $f_{\text{DIG,up}}$ ' are the upper and lower limit of the DIG. $3\sigma_{\Sigma(\text{H}\alpha)}$ is the $\Sigma_{\text{H}\alpha}$ cut-off performed for each galaxy in units of $\log \text{ erg} \cdot \text{s}^{-1} \cdot \text{kpc}^{-2}$. 'Bin size (pc)' is the average bin size of the galaxy. The last row indicates the average values of the subsample.

⁶ We are assuming that the average number of photons per recombination is 0.46 for this estimation.

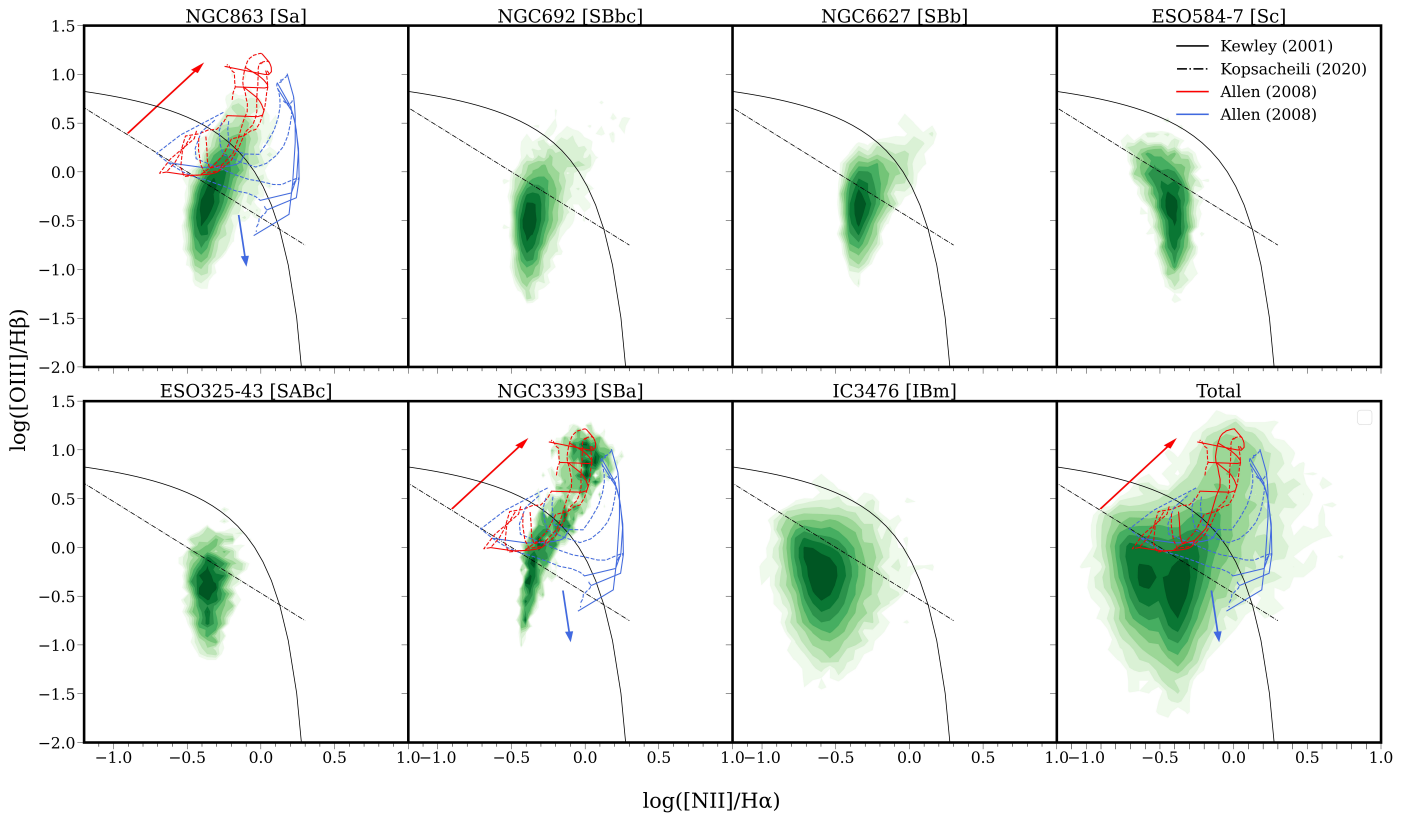


Fig. 12. BPT Diagnosis of the subsample for the DIG bins that verifies that the relative errors of [O III] line bins are below 40% and its SN above 3. The last panel displays the seven prior panels together. The central parts of NGC863, NGC3393, and NGC692 were excluded in all panels due to their strong AGN emissions. Each contour encloses the 10% of the points, being every point a single bin. Black lines are given by Kewley et al. (2001) (solid) and Kauffmann et al. (2003) (dashed) for the classic H II regions photoionisation and AGN demarcations. The dashed-dot line depicts one of the 2D diagnostics developed by Kopsacheili et al. (2020) for the separation of shock excited (e.g. supernova remnants) from photoionized regions (e.g. H II regions). Coloured lines represent the models of photoionisation by fast shocks from Allen et al. (2008). The blue and red models illustrate photoionisation where only front shocks occur and when pre-ionisation by a precursor is taken into account. The solid model curves plotted represents shocks winds of 200, 400, 500 and 1000 km/s, and dashed model curves represents magnetic field intensities of 0.0001, 1.0, 5.0 and 10. Red and blue arrows represent the direction of increasing wind velocity in each model.

4.3. BPT diagnosis of the DIG

We can explore the location of the DIG bins in the classical [N II] BPT diagram, as shown in Fig. 12. To ensure the robustness of our analysis, we exclusively consider DIG bins with a relative error of 40% or lower for the [O III], [N II], and H β lines, and a SN greater than 3. We also exclude the central part of those exhibiting an AGN: NGC863, NGC692 and NGC3393. Those constraints leave us with 80% of the DIG bins. In the same fig we have included a diagnostic from Kopsacheili et al. (2020) for the separation of shock excited from photoionized regions. The BPT of the global sample shows the DIG falls mostly below the Kewley et al. 2001 demarcation, showing a photoionisation feature due to H II regions, but with high-excitation regions above the demarcation corresponding to AGN-like emission, as previous studies noticed, usually explained as photoionisation due to HOLMES (Lac18; Bel22). However, when performing this diagnosis for individual galaxies, only NGC863 and NGC3393, both Seyfert-2 AGNs, exhibit line ratios characteristic of AGN emission. All the DIG for the rest of the galaxies show photoionisation feature due to H II regions. The central region of NGC863 and NGC3393 is not considered in this analysis, so the AGN outflows could be the source of the gas ionisation with high-excitation lines found in the BPTs. We compare our results with the theoretical models of gas highly excited through fast-shocks of Allen et al. (2008), assuming solar metallicity and a pre-shock

density of 1 cm^{-3} . We plot the predicted line ratios including (blue lines) a photoionisation by a precursor, and given a range of shock velocities (v_s) and magnetic field intensities (B). The line ratios observed in NGC863 are consisted with fast-shock without precursor with v_s between 200 and 500 km/s and B between 0.0001 and 5. In the case of NGC3393, the ratios observed corresponds to fast-shock without precursor with v_s between 200 and 1000 km/s and B between 0.0001 and 10. Furthermore, the fact that the ionisation bi-cone of NGC3393 and its continuum emission are uncoupled (Maksym et al. 2016), along with the emission line ratios in the BPT diagram indicative of ionisation by fast shocks, suggests that we are tracing gas outflows rather than DIG emission (López-Cobá et al. 2020).

The presence of AGN outflows affects the overall BPT diagnosis, revealing that a section of the DIG is ionised by sources separate from the photon leakage originating from H II regions, but what we are introducing is the ionisation cone of the AGNs, mimicking the DIG emission. Therefore, when conducting a comprehensive diagnostic assessment of the DIG across a global sample, it is crucial to completely exclude galaxies that exhibit AGN emission. This occurs even if the whole DIG is ionised by star-forming regions, as observed in the remaining galaxies in the subsample. This effect also explains the high $\Sigma_{H\alpha}$ in the DIG found in the same two galaxies; NGC863 and NGC3393, as we are incorporating the AGN emissions.

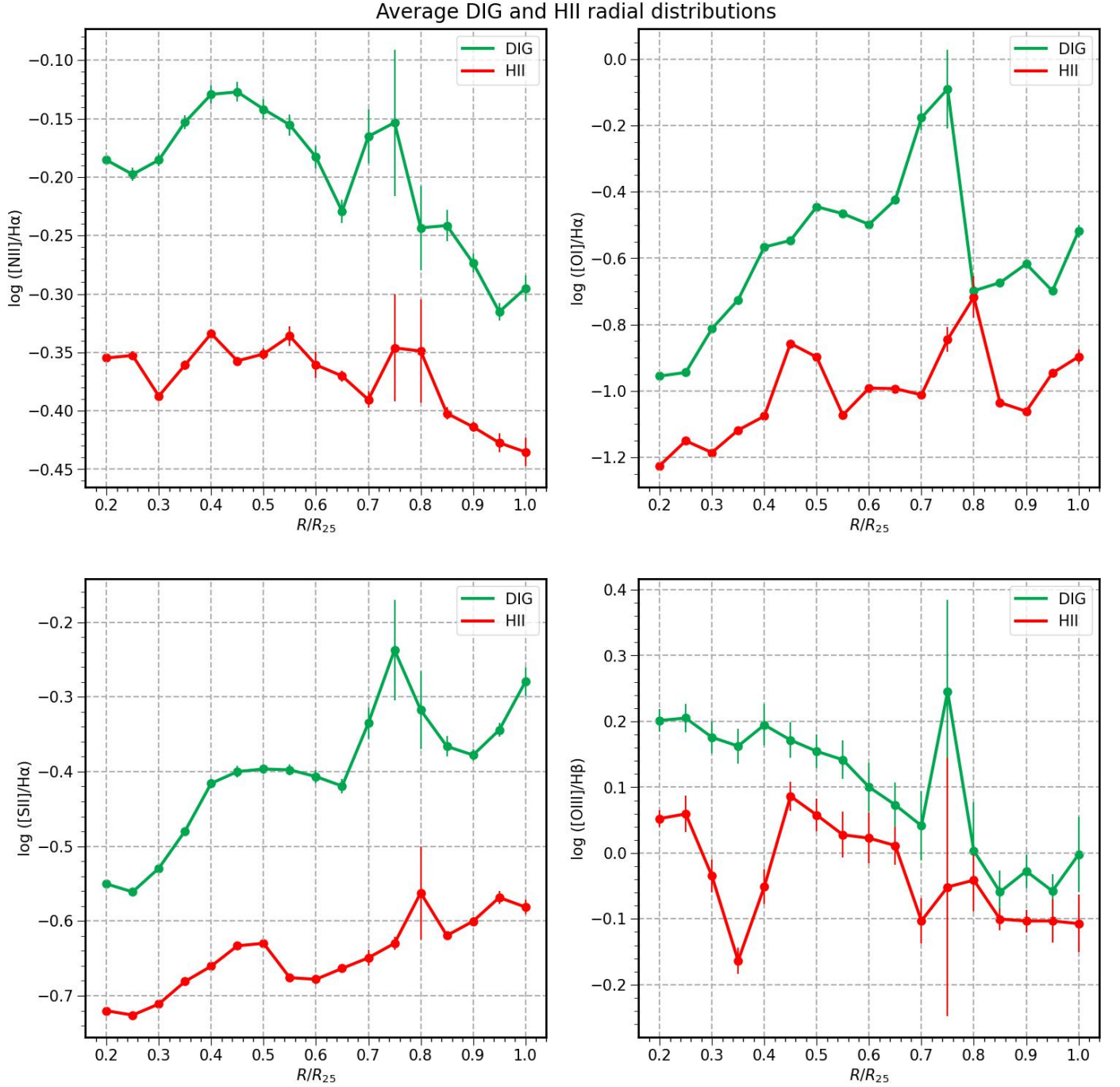


Fig. 13. Radial distribution of the $[S II]/H\alpha$ ratio of the DIG bins (green), and HII regions according to our definition (red), obtained as the ratio of the mean values of the respective fluxes within a ring of width $0.05R_{25}$ with a step of $0.05R_{25}$ from $0.2R_{25}$ to R_{25} . We are only considering those bins whose relative error in $[S II]$ and $H\alpha$ lines are lower than 40%. To avoid the strong AGN emissions, we start all the distributions from $0.2R_{25}$. In general we see a tendency to increase the ratio as we move to outer regions of the galaxy. Besides, the ratio is in all cases higher in DIG regions, as we expected from the literature (Haffner et al. 2009b).

4.4. DIG line ratios

Further evidence of the connection between the DIG and HII regions lies in the behaviour of the $[S II]/H\alpha$, $[N II]/H\alpha$, $[O I]/H\alpha$ and $[O III]/H\beta$ ratios.

An observational fact is that the low-ionisation $[N II]/H\alpha$ and $[S II]/H\alpha$ line ratios increase with decreasing $\Sigma_{H\alpha}$, the best example being the increase in these line ratios with increasing distance from the mid-plane, both in the Milky Way (Haffner et al. 1999) and other galaxies (Rand 1999; Tüllmann et al. 2000). Al-

though the values for $[N II]/H\alpha$ and $[S II]/H\alpha$ could vary considerably in the DIG, they are correlated, often with a nearly constant $[S II]/[N II]$ ratio over large regions (Haffner et al. 2009b). Nevertheless, there is a significant lack of studies that have examined the variations of the DIG line ratios in terms of their galactocentric distance dependence.

Fig. 13, shows the average radial distribution of the $[S II]/H\alpha$, $[N II]/H\alpha$, $[O III]/H\beta$ and $[O I]/H\alpha$ line ratios for the lower DIG limit. The distributions have been generated using the same method as for $\Sigma_{H\alpha}$ (as shown in Fig. 11) and f_{DIG}

(blue curves of the Fig. 10) radial distributions. Each data point is computed as the average value from the seven galaxies in the subsample at a specific radius. We create these distributions for both the DIG (in green) and the area corresponding to H II regions (red). In all instances, we exclusively consider the bins with a relative error below 40% for each line.

In all cases, the DIG line ratios show higher values than the line ratios corresponding to the H II regions.

The [N II]/H α radial distributions (upper-left panel), for both the DIG and the H II regions, decrease with galactocentric distance. The [N II]/H α DIG distribution ranges from 0.67 to 0.51, while for the H II regions from 0.44 to 0.37 between $0.2R_{25}$ and $1R_{25}$, being the [N II]/H α line ratio of the DIG 0.15 dex higher in average. The [N II]/H α line ratio is a well-know metallicity indicator (Storchi-Bergmann et al. 1994; Denicoló et al. 2002; Ho et al. 2015); thus, the decreasing value as a function of radius is primarily reflecting a change in metallicity of the ionised gas, in this case of the metallicity gradient of the spiral galaxies. Nevertheless, given that N⁺/N and H⁺/H vary little within the DIG, for a given metallicity, variations in the [N II]/H α line ratio essentially trace variations in T_e (Haffner et al. 2009b). However, calculating absolute temperatures is uncertain because of the requisite assumptions about the precise ionic fractions and elemental abundances.

Fig. 13 suggest a flattening in the [N II]/H α index in both the H II regions and the DIG distributions for $r < 0.6R_{25}$, indicating a potential contribution from the DIG to the observed radial metallicity gradients within galactic planes (Z17).

On the other hand, the [S II]/H α line ratio increases radially in both H II regions and DIG regimes (lower-left panel of Fig. 13), with higher values observed in the DIG; from 0.28 to 0.63 for the DIG and from 0.19 to 0.12 for the H II regions between $0.2R_{25}$ and $1R_{25}$, being the [S II]/H α DIG line ratio higher by 0.15 dex in average. The shapes of both distributions display comparable patterns, reaching a maximum at $0.75\text{--}0.8R_{25}$.

The [O I] line is produced by collisions of neutral oxygen with thermal electrons, its intensity is a measure of the neutral hydrogen content within the DIG. The first ionisation potential of the oxygen is close to that of the hydrogen, and the large H⁺+O⁰ \leftrightarrow H⁰+O⁺ charge-exchange cross section keeps O⁺/O nearly equal to to H⁺/H. Thus, the [O I]/H α ratio is related to the amount of H⁰ relative to H⁺, and it is a sensitive probe of the ionisation state of the emitting gas (Reynolds et al. 1998; Haffner et al. 2009b). The volume photon emissivity ϵ of the O ¹D $\lambda 6300$ transition relative to H α is related to the hydrogen ionisation ratio $n(\text{H}^+)/n(\text{H}^0)$, with a linear dependence of the gas-phase abundance of oxygen $n(\text{O})/n(\text{H})$ and a weak dependence that tracks changes in T_e (Haffner et al. 2009b). Observations of [O I] in the Milky Way and objects at $z \sim 0$ are difficult because of the [O I] $\lambda 6300$ air glow line, which is of order 100 times brighter than the interstellar line. Voges & Walterbos (2006) made the first DIG detection of [O I] $\lambda 6300$ in any non-edge-on spiral other than the Milky Way near the H II region NGC 604 in M33, with observed [O I]/H α ratios in the range 0.038 – 0.097. In the upper-right panel of Fig. 13, we observe the azimuthally averaged values of the [O I]/H α ratio with a significantly steeper slope in the DIG compared to the emission in the H II regions, increasing from 0.12 to 0.79 between $0.25R_{25}$ to $0.75R_{25}$ (-0.9 to -0.1 in log), while the H II distribution increases from 0.06 to 0.18 (-1.2 to -0.7 in log), which are higher than the values reported by Voges & Walterbos (2006) for M33, and higher than the values found by Bel22 with an upper limit ~ 0.3 . The high [O I]/H α line ratio in the DIG found in the

BETIS showcase sample is challenging, and will be matter of study in forthcoming studies.

The radial distribution of the [O III]/H β line ratio is shown in the lower-right panel of Fig. 13. Generally, the variation in this ratio between DIG and H II regions relies on the specific physical characteristics of the ISM (Z17). Normal spiral galaxies show an increasing value of the [O III]/H β line ratio with increasing radius, mainly due to secondary dependence on metallicity, with a high dispersion in the central regions (~ 1 dex for $r < 0.4R_{25}$). Previous studies also show a [O III]/H β ratio both higher in H II regions (Greenawalt et al. 1997; Galarza et al. 1999) and lower than the DIG regions (Collins & Rand 2001; Otte et al. 2002). In our subsample, this ratio remains elevated in DIG regions, but the difference between the DIG and H II distributions is less pronounced compared to the other line ratio distributions. This trend suggests a radial decrease in this ratio; from 1.58 to 1.0 in the DIG (0.2 to 0.0 in log) and from 1.07 to 0.79 in the H II regions (0.05 to -0.1 in log). Our results indicate that these line ratios are typically higher in the DIG compared with the H II regions. This trend aligns with what is commonly reported in the existing literature (Haffner et al. 2009b).

The similarity in the trends observed in the radial distribution of $\Sigma_{H\alpha}$ and line ratios between both DIG and H II regions, especially in the case of [N II]/H α and [S II]/H α ratios, along with the majority of DIG bins falling within the photoionisation regime on the BPT diagram, suggests that the explanation for DIG behaviour can be attributed to photoionisation processes within the galactic plane, without the need for alternative sources of ionisation.

However, another phenomena needs to be explained, the low values of EW(H α) found in the DIG, specially in regions with photoionisation regimes not corresponding to SF regions (Lac18; Bel22).

4.5. EW(H α) in the DIG

The EW(H α) has been used by many authors to differentiate between ionisation caused by star formation and AGN, and ionisation caused by a smooth background of hot evolved stars. Cid Fernandes et al. (2011) used SDSS data to demonstrate that the emission-line galaxy population exhibits a bimodal distribution in EW(H α), and that 3 Å serves as an empirical demarcation between these two. Later, Belfiore et al. (2016) using MaNGA data, showed the presence of extended (kpc scale) low-ionisation emission-line regions (LIERs) in both star-forming and quiescent galaxies, associated with low EW(H α) (< 3 Å). In SF galaxies, the LIER emission was associated with diffuse ionised gas, most evident as extraplanar emission in edge-on systems.

Lac18 proposed a separation of DIG ionisation regimes based on the EW(H α) and applied over all types of galaxies, including elliptical and S0. The regions where EW(H α) > 14 Å traces SF regime, 3 < EW(H α) < 14 Å reflects a mixed regime, and regions where EW(H α) < 3 Å define the component of the DIG where photoionisation is dominated by hot, low-mass, evolved stars (HOLMES; Flores-Fajardo et al. 2011; Cid Fernandes et al. 2011). Those stars were proposed as an additional ionisation source of the DIG, in order to explain the high [O III]/H β ratio found in the extraplanar DIG in edge-on galaxies (Reynolds et al. 1998; Rand 1999; Flores-Fajardo et al. 2011).

The significance of employing the EW(H α) to distinguish between various ionisation sources, while considering the contribution of HOLMES to the energy budget, has been a topic of fre-

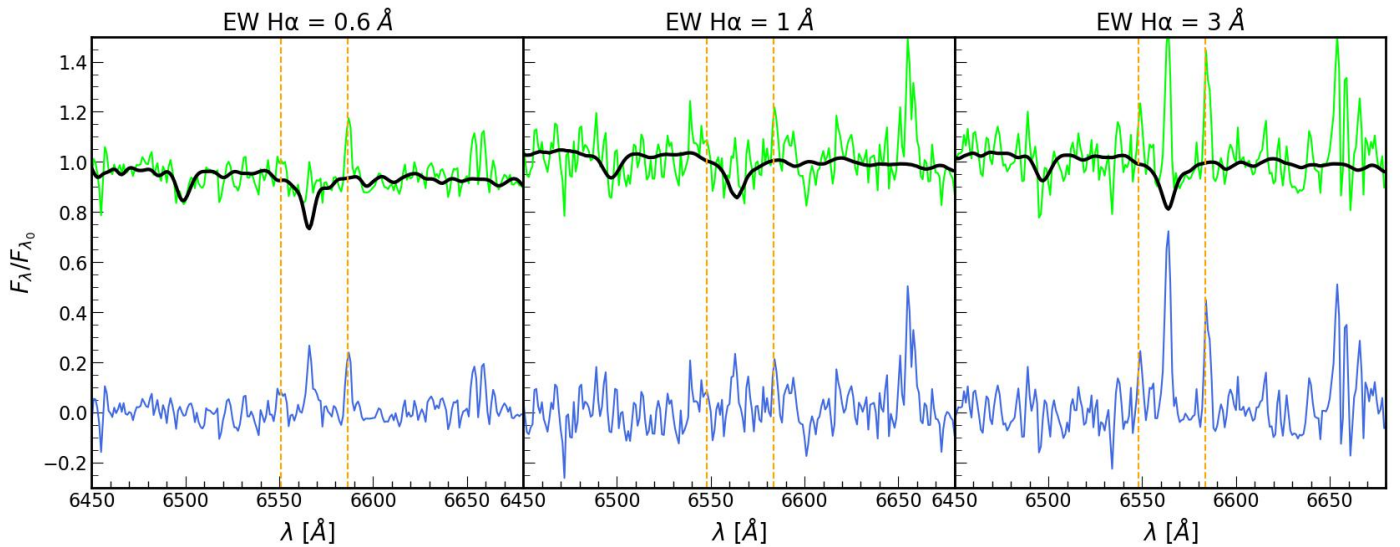


Fig. 14. Three examples of observed (green), model (black) and nebular (blue) spectra of different $EW(H\alpha) = 0.6, 1$ and 3 \AA . All observed spectra are integrated spectra from NGC863 bins, the model spectra are obtained from STARLIGHT following our methodology and the nebular spectra are obtained subtracting the model to the observed (see text). Gold lines represent the $[N II]$ doublet.

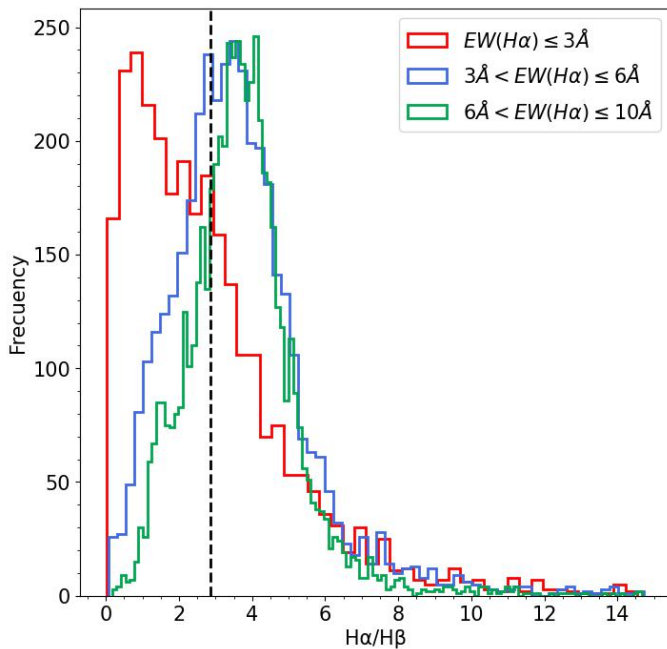


Fig. 15. Distribution of $H\alpha/H\beta$ ratio for three different $EW(H\alpha)$ regimes. Each distribution represent the $H\alpha/H\beta$ flux ratio for all bins between $6\text{ \AA} < EW(H\alpha) \leq 10 \text{ \AA}$ (green), $3\text{ \AA} < EW(H\alpha) \leq 6 \text{ \AA}$ (blue), and $EW(H\alpha) \leq 3 \text{ \AA}$ (red), for the seven binned galaxies listed in Table 1. Black vertical dashed line presents the theoretical ratio of $H\alpha/H\beta = 2.87$ (Osterbrock & Ferland 2006). We can see that a substantial part of the bins with $EW(H\alpha) \leq 3 \text{ \AA}$ shows a non-physical ratio (< 2.87).

quent discussion among several authors, even in the context of face-on galaxies (e.g. Cid Fernandes et al. 2011; Lac18; Bel22), not being clear yet the true division (if exists) between ionisation carried by HOLMES, star formation or shocks. Moreover, Bel22 also noticed an unclear division for ionisation by HOLMES at $EW(H\alpha) = 3 \text{ \AA}$ and by star formation at $EW(H\alpha) = 14 \text{ \AA}$ sug-

gested by Lac18, since their $EW(H\alpha)$ for DIG and H II regions tends to overlap in lower $EW(H\alpha)$ regimes.

However, the general methodology employed in IFS studies in order to measure both the line intensities and the equivalent width of Balmer recombination lines poses a problem for spectra with low SN of the emission lines. This methodology implies measuring the line intensities and EWs from a nebular spectrum obtained from subtracting a fitted stellar model to the observed spectrum. In the case of the Balmer recombination lines, this procedure typically makes a small correction to the emission line intensity due to the underlying stellar absorption. For $EW(H\alpha) > 3 \text{ \AA}$, this correction is usually of a few percent. Nevertheless, when the SN of the $H\alpha$ line is ~ 1 ($H\alpha$ emission embedded in the stellar continuum), the resulting $H\alpha$ emission, and therefore $EW(H\alpha)$, would depend on the Balmer stellar absorption feature due to the SSP fitting. In this case, the underlying stellar absorption would not represent just a correction of the emission line, but the resulting flux would be fully originated from the fitted stellar spectrum, generating low $EW(H\alpha)$ values $\lesssim 3 \text{ \AA}$.

This is shown in Fig. 14, where we plot the observed (green), fitted stellar model (black) and nebular (blue) spectra of regions with $EW(H\alpha)$ of 0.6, 1 and 3 \AA . In the left and central panels the $H\alpha$ emission in the observed spectra is totally embedded by the stellar continuum. However, due to the fitted stellar model, the nebular spectra includes a $H\alpha$ emission line of the same magnitude that the stellar absorption feature of the model, from which an $EW(H\alpha)$ of 0.6 \AA (left) and $EW(H\alpha) = 1 \text{ \AA}$ (right) are measured. On the other hand, the right panel of Fig. 14 shows that for a region with $EW(H\alpha) = 3 \text{ \AA}$, the underlying stellar absorption of the model makes just a small correction to the total flux of the emission line.

Consequently, when the SN of the $H\alpha$ is ~ 1 and/or when the emission is embedded in the stellar continuum ($EW(H\alpha) \lesssim 3 \text{ \AA}$), the resulting $EW(H\alpha)$ is dependent on the selection of SSPs and the fitting methodology. This sharp differentiation between HOLMES dominated regions, as well as the differentiation between LIERs and passive galaxies (Cid Fernandes et al. 2011;

Belfiore et al. 2016) may not be reliable, as it could potentially originate from a methodological artefact.

Further evidence that the low $EW(H\alpha)$ regime ($\lesssim 3 \text{ \AA}$) imposes a methodological challenge is manifested when verifying the validity of physical parameters derived from the embedded emission lines, such as the $H\alpha/H\beta$ Balmer decrement. Fig. 15 shows the distribution of the $H\alpha/H\beta$ ratio for different $EW(H\alpha)$ regimes, while for $EW(H\alpha) > 3 \text{ \AA}$ the distributions peak at the theoretical $H\alpha/H\beta$ ratio $\gtrsim 2.87$ (Osterbrock & Ferland 2006), for the regions with $EW(H\alpha) < 3 \text{ \AA}$, the ratio shows non physical values.

In addition, the values of $EW(H\alpha) < 14 \text{ \AA}$ and $< 3 \text{ \AA}$ are not exclusive to the DIG emission, so the demarcation with H II regions using the $EW(H\alpha)$ is not clear (Bel22). This is also evident in Fig. 16, which shows the distribution of $EW(H\alpha)$ for both DIG and H II bins within our subsample. We found that the galaxies with lower median $EW(H\alpha)$ in the DIG regions ($\sim 9 \text{ \AA}$) are NGC863 and NGC3393, both Sa type, followed by NGC692 (Sbc), NGC6627 (Sb) and ESO325-43 (Sc), with $EW(H\alpha) \sim 18 - 20 \text{ \AA}$. ESO584-7 (Sc) and IC3476 (Im) have exceptionally high $EW(H\alpha)$ in the DIG regions, with 34 and 36 \AA respectively. ESO584-7 is a H II galaxy (Contini et al. 1998), thus, the high luminosity and star formation rate may be the cause of this high median $EW(H\alpha)$. The case of IC3476 is also special. It is a galaxy suffering the effects of the ram pressure stripping due to the Virgo Cluster intergalactic environment (Boselli et al. 2021). These authors show that the effects of this perturbations reach scales of individual H II regions $r_{eq} \sim 50 \text{ pc}$. Furthermore, the compression of the gas along its stellar disc may be the cause of the increase of the star formation activity. This increment could explain the exceptionally high $EW(H\alpha)$ in the DIG regions found in this galaxy, as happened with ESO584-7.

In general, this results are in concordance with previous authors (Lac18; Bel22), being the early type galaxies those with lower $EW(H\alpha)$, due to the older stellar populations of their bulges, and late-types those with higher $EW(H\alpha)$. The median $EW(H\alpha)$ of the DIG regions for all subsample is $\sim 25 \text{ \AA}$, substantially higher in comparison with previous studies ($\sim 5 \text{ \AA}$) due to the bias given by ESO584-7 and IC3476, and due to the small subsample selected.

4.6. Dust reddening in the DIG regime

In Fig. 17 we show the reddening in the DIG bins, obtained as the radial distribution of the $H\alpha/H\beta$ ratio for the 7 galaxies of our subsample. This ratio is always lower in the DIG regime (between 3.85 and 2.5), following the same tendency to decrease radially as in the H II regions, with ratio between 4 and 3.25. The decline of the $H\alpha/H\beta$ ratio in DIG regimes shown are in concordance to the expectations. Since the $H\alpha/H\beta$ ratio reflects the attenuation of young stars by dust both in H II regions and in the ISM (Chevallard et al. 2013), is expected the ratio to be lower in the DIG, due to the lower optical depth and the increased scatter in the dust attenuation-line luminosity relation (Vale Asari et al. 2020). The fact that we find a $H\alpha/H\beta$ ratio lower in the DIG than in the H II regions evidences that the DIG temperature is warmer than the H II regions (Osterbrock & Ferland 2006), that is also consistent with the temperatures found in the WIM ($\sim 2000 \text{ K}$ warmer than H II regions, Madsen & Reynolds 2005).

5. Summary and conclusions

In this work, we present the Bidimensional Exploration of the warm-Temperature Ionised gaS (BETIS) project, designed for the spatially resolved and spectral study of the Diffuse Ionised Gas (DIG) in a selection of nearby galaxies. We present a methodology to characterize and study spatial and spectroscopically the DIG using a sample of 265 galaxies selected from the AMUSING, AMUSING+ and AMUSING++ projects. After performing a selection criteria based on data quality and the spatial resolution of the datacubes, the final BETIS sample consist in 265 star-forming galaxies with different morphologies, including irregulars, mergers, LINERs and seyferts at $z < 0.06$. The median spatial FWHM of the BETIS sample is $\sim 275 \text{ pc}$. This resolution falls between the 0.8 kpc resolution of CALIFA and the roughly 50 pc resolution of the 19 galaxies in PHANGS-MUSE.

We selected a showcase subsample consisting of 7 galaxies with diverse morphological and characteristic traits to validate our methodology for characterizing the DIG. This methodology involves the following steps:

- An adaptive binning is performed to the observed datacube in order to increase the SN of the fainter lines such as [O III], [O I] and [S II]. Our technique is based on the spectroscopic SN of the [S II] line, with a target SN of 10.
- We conduct a Single Stellar Population (SSP) synthesis using the STARLIGHT code for each integrated spectrum within the binned datacube. Subsequently, we employ Gaussian fitting to the residuals of each SSP fitting to derive the binned emission line maps for the 9 lines of interest. Additionally, we generate a binned $EW(H\alpha)$ map.
- The DIG is separated from the H II regions using a combination of an automated tool to detect and subtract the H II regions from the binned $H\alpha$ maps, and a cut-off in $H\alpha$ surface brightness to subtract bright, irregular H II regions not detected by the automated tools.

We find an average DIG fraction of 40%-70% in the showcase subsample, being NGC3393 the one with the higher DIG fraction (69%-87%), followed by NGC863, ESO325-43, NGC692, NGC6627, ESO584-7, and IC3476. Those with higher DIG fraction are the two Seyfert of the sample, NGC3393 and NGC863. This is further exemplified when analysing the radial distributions of the $\Sigma_{H\alpha}$ in the DIG and H II regions. In these two galaxies, the DIG exhibits higher surface brightness compared to the H II regions, with the disparity between these two regimes reaching up to 1 dex. The overall radial distributions of $\Sigma_{H\alpha}$, as depicted in Fig. 11, generally reveal similar trends for both H II regions and DIG, with a radial decrease. However, there is an increase in $\Sigma_{H\alpha}$ within the bars of NGC692 and NGC6627 for the H II regions.

On average, we observe in Fig. 13 higher [S II]/ $H\alpha$, [N II]/ $H\alpha$, [O III]/ $H\beta$, and [O I]/ $H\alpha$ ratios in the DIG compared to the H II regions. Additionally, the radial trends of the DIG and H II distributions are similar in all cases, indicating a correlation between the ionisation of these species in both the DIG and the H II regions.

Computing the [N II] BPT diagram also highlights a significant distinction between the two Seyfert galaxies and the rest of the subsample. It is evident that the DIG is predominantly photoionised by H II regions in all galaxies, except for NGC3393 and NGC863. In these two cases, the ionisation source of the DIG appears to be accounted for by the fast shock models proposed by Allen et al. (2008). Nevertheless, it is worth noting

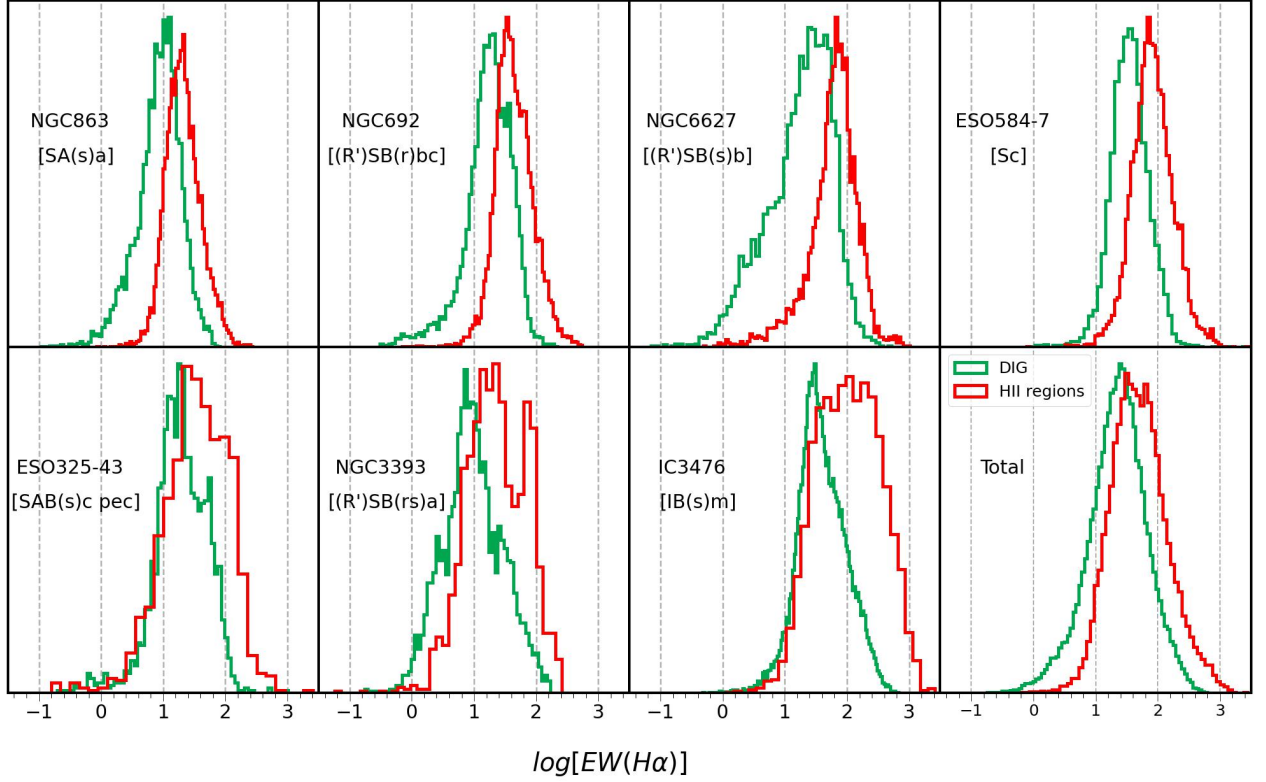


Fig. 16. $\text{EW}(\text{H}\alpha)$ distributions for all bins of the subsample. Green histograms represents the distribution for the DIG emission bins, and red for the H II regions emission bins. Last histogram represent the distribution for the 7 galaxies.

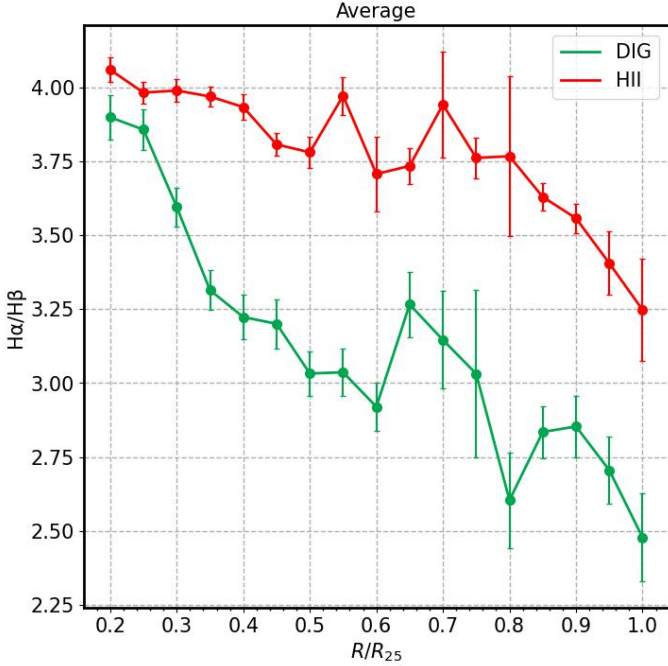


Fig. 17. Mean radial $\text{H}\alpha/\text{H}\beta$ ratio distribution of the subsample. The distributions are obtained as in Fig. 13. Red represent the distribution for the H II regions bins, and green for the DIG bins. Both distributions decrease radially in average, but the extinction is always lower in the DIG regime.

that these two galaxies host prominent AGNs, which can mimic the emission of the DIG when assessing a global BPT for the entire sample. This can create a misleading impression of high-

ionisation line regions within the DIG powered by sources other than star formation.

We also addressed the challenge of employing the $\text{EW}(\text{H}\alpha)$ as a proxy for delineating DIG regions and different ionisation regimes. This issue arises because at low $\text{EW}(\text{H}\alpha)$, typically used to identify HOLMES or AGNs regimes, the $\text{H}\alpha$ line derived from synthetic spectra after conducting a SSP fitting can be an artifact of the model. This results in an artificial $\text{H}\alpha$ emission line when correcting the observed $\text{H}\alpha$ emission with the stellar model absorption, after subtracting the model from an observed $\text{H}\alpha$ line with a spectroscopic $\text{SN} \sim 1$. Therefore, the low $\text{EW}(\text{H}\alpha)$ can be a result of the characteristics of the stellar models, making it dependent on these models if we do not consider the spectroscopic SN ratio of the observed $\text{H}\alpha$.

The distributions of $\text{EW}(\text{H}\alpha)$ for the DIG regions in our subsample exhibit a morphological pattern. Sa-type galaxies, with prominent bulges of older stellar populations, have lower $\text{EW}(\text{H}\alpha)$. They are followed by Sb and Sc galaxies. Notably, ESO584-7 and IC3476 show significantly higher EWs. ESO584-7 is an [N II] galaxy, while IC3476 experiences elevated EWs due to ram pressure stripping in the Virgo Cluster's intergalactic environment.

Lastly, we examined the impact of dust reddening in the DIG by assessing the radial distribution of $\text{H}\alpha/\text{H}\beta$ ratios within both the DIG and H II regions across our entire subsample. Our results shows that extinction is consistently lower in DIG regions, indicating that the DIG presents warmer temperatures than the H II regions, as previous authors found in the WIM.

It is essential to note that these results are preliminary, as they are based on a small subsample of seven galaxies drawn from the BETIS dataset of 265 galaxies. In the forthcoming studies of this series, we will expand the analysis to the entire sample in order to mitigate potential biases, we will explore how the re-

sults and methodology may vary based on galaxy morphology and inclination (edge-on). We will also investigate the influence of the DIG on the determination of various parameters, including chemical abundances and star formation rate. Additionally, we will explore other spectroscopic lines of interest for the DIG study, such the high-excitation He I, aiming to uncover potential new ionisation mechanisms of the DIG.

Acknowledgements. R.G.D. acknowledges the CONAHcyT scholarship No. 1088965 and INAOE for the PhD program. The authors also acknowledges Laboratorio Nacional de Supercómputo del Sureste de México (LNS) for allowing the usage of their cluster with the project No. 202201027C in collaboration with INAOE, and Itziar Aretxaga for allowing us the usage of the Toltec/GTM cluster. L.G. acknowledges financial support from the Spanish Ministerio de Ciencia e Innovación (MCIN), the Agencia Estatal de Investigación (AEI) 10.13039/501100011033, and the European Social Fund (ESF) "Investing in your future" under the 2019 Ramón y Cajal program RYC2019-027683-I and the PID2020-115253GA-I00 HOSTFLOWS project, from Centro Superior de Investigaciones Científicas (CSIC) under the PIE project 20215AT016, and the program Unidad de Excelencia María de Maeztu CEX2020-001058-M. The data of this work were obtained at the European Southern Observatory under the ESO programmes between 095.D-0091 and 0103.B-0834. The images of Fig 9 were created with the help of the NOIRLab/IPAC/ESA/STScI/CFA FITS Liberator and the free web-based image editor photopea.com

References

- Allen M. G., Groves B. A., Dopita M. A., Sutherland R. S., Kewley L. J., 2008, *ApJS*, **178**, 20
- Bacon R., et al., 2010, in McLean I. S., Ramsay S. K., Takami H., eds, Society of Photo-Optical Instrumentation Engineers (SPIE) Conference Series Vol. 7735, Ground-based and Airborne Instrumentation for Astronomy III. p. 773508 ([arXiv:2211.16795](https://arxiv.org/abs/2211.16795)), doi:10.1117/12.856027
- Baldwin J. A., Phillips M. M., Terlevich R., 1981, *PASP*, **93**, 5
- Belfiore F., et al., 2016, *MNRAS*, **461**, 3111
- Belfiore F., et al., 2022, *A&A*, **659**, A26
- Berkhuijsen E. M., Mitra D., Mueller P., 2006, *Astronomische Nachrichten*, **327**, 82
- Bertin E., Arnouts S., 1996, *A&AS*, **117**, 393
- Binette L., Flores-Fajardo N., Raga A. C., Drissen L., Morisset C., 2009, *ApJ*, **695**, 552
- Birk G. T., Lesch H., Neukirch T., 1998, *MNRAS*, **296**, 165
- Boquien M., Buat V., Perret V., 2014, *A&A*, **571**, A72
- Boselli A., et al., 2021, *A&A*, **646**, A139
- Bruzual A. G., 2007a, in Vazdekis A., Peletier R., eds, Vol. 241, Stellar Populations as Building Blocks of Galaxies. pp 125–132 ([arXiv:astro-ph/0703052](https://arxiv.org/abs/astro-ph/0703052)), doi:10.1017/S1743921307007624
- Bruzual G., 2007b, in Vallenari A., Tantalo R., Portinari L., Moretti A., eds, Astronomical Society of the Pacific Conference Series Vol. 374, From Stars to Galaxies: Building the Pieces to Build Up the Universe. p. 303 ([arXiv:astro-ph/0702091](https://arxiv.org/abs/astro-ph/0702091)), doi:10.48550/arXiv.astro-ph/0702091
- Bruzual G., Charlot S., 2003, *MNRAS*, **344**, 1000
- Bundy K., et al., 2015, *ApJ*, **798**, 7
- Cappellari M., Copin Y., 2003, *MNRAS*, **342**, 345
- Cardelli J. A., Clayton G. C., Mathis J. S., 1989, *ApJ*, **345**, 245
- Ceverino D., Klypin A., 2008, in Bureau M., Athanassoula E., Barbu B., eds, Vol. 245, Formation and Evolution of Galaxy Bulges. pp 33–34 ([arXiv:0710.1666](https://arxiv.org/abs/0710.1666)), doi:10.1017/S1743921308017213
- Ceverino D., Klypin A., 2009, *ApJ*, **695**, 292
- Chabrier G., 2003, *PASP*, **115**, 763
- Chevallard J., Charlot S., Wandelt B., Wild V., 2013, *MNRAS*, **432**, 2061
- Cid Fernandes R., Mateus A., Sodré L., Stasińska G., Gomes J. M., 2005, *MNRAS*, **358**, 363
- Cid Fernandes R., Stasińska G., Schlickmann M. S., Mateus A., Vale Asari N., Schoenell W., Sodré L., 2010, *MNRAS*, **403**, 1036
- Cid Fernandes R., Stasińska G., Mateus A., Vale Asari N., 2011, *MNRAS*, **413**, 1687
- Collins J. A., Rand R. J., 2001, *ApJ*, **551**, 57
- Congiu E., et al., 2023, *A&A*, **672**, A148
- Contini T., Considere S., Davoust E., 1998, *A&AS*, **130**, 285
- Della Bruna L., et al., 2022a, *A&A*, **660**, A77
- Della Bruna L., et al., 2022b, *A&A*, **666**, A29
- Denicoló G., Terlevich R., Terlevich E., 2002, *MNRAS*, **330**, 69
- Detmar R. J., 1990, *A&A*, **232**, L15
- Emsellem E., et al., 2022, *A&A*, **659**, A191
- Erroz-Ferrer S., et al., 2019, *MNRAS*, **484**, 5009
- Espinosa-Ponce C., Sánchez S. F., Morisset C., Barrera-Ballesteros J. K., Galbany L., García-Benito R., Lacerda E. A. D., Mast D., 2020, *MNRAS*, **494**, 1622
- Ferguson A. M. N., Wyse R. F. G., Gallagher J. S. I., Hunter D. A., 1996a, *AJ*, **111**, 2265
- Ferguson A. M. N., Wyse R. F. G., Gallagher J. S., 1996b, *AJ*, **112**, 2567
- Finkbeiner D. P., 2003, *ApJS*, **146**, 407
- Fitzpatrick E. L., 1999, *PASP*, **111**, 63
- Flores-Fajardo N., Morisset C., Stasińska G., Binette L., 2011, *MNRAS*, **415**, 2182
- Gadotti D. A., et al., 2019, *MNRAS*, **482**, 506
- Gaensler B. M., Madsen G. J., Chatterjee S., Mao S. A., 2008, *PASA*, **25**, 184
- Galarza V. C., Walterbos R. A. M., Braun R., 1999, *AJ*, **118**, 2775
- Galbany L., et al., 2016, *MNRAS*, **455**, 4087
- Gatto A., et al., 2017, *MNRAS*, **466**, 1903
- Grasha K., 2022, *arXiv e-prints*, p. [arXiv:2211.06005](https://arxiv.org/abs/2211.06005)
- Greenawalt B., Walterbos R. A. M., Braun R., 1997, *ApJ*, **483**, 666
- Gridale K. M., 2017, PhD thesis, University of Surrey, UK
- Guélin M., 1974, in Kerr F. J., Simonson S. C., eds, Vol. 60, Galactic Radio Astronomy. p. 51
- Haffner L. M., Reynolds R. J., Tuftes S. L., 1999, *ApJ*, **523**, 223
- Haffner L. M., et al., 2009a, *Rev. Mod. Phys.*, **81**, 969
- Haffner L. M., et al., 2009b, *Reviews of Modern Physics*, **81**, 969
- Hewish A., Bell S. J., Pilkington J. D. H., Scott P. F., Collins R. A., 1968, *Nature*, **217**, 709
- Hidalgo-Gómez A. M., 2005, *A&A*, **442**, 443
- Hills J. G., 1974, *ApJ*, **190**, 109
- Ho I. T., Kudritzki R.-P., Kewley L. J., Zahid H. J., Dopita M. A., Bresolin F., Rupke D. S. N., 2015, *MNRAS*, **448**, 2030
- Hoopes C. G., Walterbos R. A. M., 2003, *ApJ*, **586**, 902
- Hopkins P. F., Kereš D., Oñorbe J., Faucher-Giguère C.-A., Quataert E., Murray N., Bullock J. S., 2014, *MNRAS*, **445**, 581
- Hoyle F., Ellis G. R. A., 1963, *Australian Journal of Physics*, **16**, 1
- Husemann B., et al., 2013, *A&A*, **549**, A87
- Husemann B., et al., 2019, *A&A*, **627**, A53
- Jones A., et al., 2017, *A&A*, **599**, A141
- Kauffmann G., et al., 2003, *MNRAS*, **346**, 1055
- Kennicutt Robert C. J., Edgar B. K., Hodge P. W., 1989, *ApJ*, **337**, 761
- Kewley L. J., Dopita M. A., Sutherland R. S., Heisler C. A., Trevena J., 2001, *ApJ*, **556**, 121
- Klessen R. S., Glover S. C. O., 2016, in Revaz Y., Jablonka P., Teyssier R., Mayer L., eds, Saas-Fee Advanced Course Vol. 43, Saas-Fee Advanced Course. p. 85 ([arXiv:1412.5182](https://arxiv.org/abs/1412.5182)), doi:10.1007/978-3-662-47890-5_2
- Kopsacheili M., Zezas A., Leonidaki I., 2020, *MNRAS*, **491**, 889
- Kulkarni S. R., Heiles C., 1987, in Hollenbach D. J., Thronson Harley A. J., eds, Vol. 134, Interstellar Processes. p. 87, doi:10.1007/978-94-009-3861-8_5
- Lacerda E. A. D., et al., 2018, *MNRAS*, **474**, 3727
- Li Z., et al., 2023, *MNRAS*, **518**, 286
- Lipovetsky V. A., Neizvestny S. I., Neizvestnaya O. M., 1988, *Soobshcheniya Spetsial'noj Astrofizicheskoy Observatorii*, **55**, 5
- López-Cobá C., et al., 2020, *AJ*, **159**, 167
- Lugo-Aranda A. Z., Sánchez S. F., Espinosa-Ponce C., López-Cobá C., Galbany L., Barrera-Ballesteros J. K., Sánchez-Menguiano L., Anderson J. P., 2022, *RAS Techniques and Instruments*, **1**, 3
- Madsen G. J., Reynolds R. J., 2005, *ApJ*, **630**, 925
- Makarov D., Prugniel P., Terekhova N., Courtois H., Vauglin I., 2014, *A&A*, **570**, A13
- Maksym W. P., Fabbiano G., Elvis M., Karovska M., Paggi A., Raymond J., Wang J., Storch-Bergmann T., 2016, *ApJ*, **829**, 46
- Minter A. H., Spangler S. R., 1997, *ApJ*, **485**, 182
- Monnet G., 1971, *A&A*, **12**, 379
- Oey M. S., et al., 2007, *ApJ*, **661**, 801
- Okabe A., Boots B., Sugihara K., Chiu S., 2000, Spatial Tessellations: Concepts and Applications of Voronoi Diagrams. Vol. 43, doi:10.2307/2687299
- Osterbrock D. E., Ferland G. J., 2006, Astrophysics of gaseous nebulae and active galactic nuclei. University Science Books
- Otte B., Reynolds R. J., Gallagher J. S. I., Ferguson A. M. N., 2001, *ApJ*, **560**, 207
- Otte B., Gallagher J. S. I., Reynolds R. J., 2002, *ApJ*, **572**, 823
- Poetrodjojo H., D'Agostino J. J., Groves B., Kewley L., Ho I. T., Rich J., Madore B. F., Seibert M., 2019, *MNRAS*, **487**, 79
- Poggianti B. M., et al., 2017, *ApJ*, **844**, 48
- Rand R. J., 1999, *ApJ*, **521**, 492
- Rand R. J., Kulkarni S. R., Hester J. J., 1990, *ApJ*, **352**, L1
- Raymond J. C., 1992, *ApJ*, **384**, 502
- Reynolds R. J., 1971, PhD thesis, University of Wisconsin, Madison
- Reynolds R. J., 1985, *ApJ*, **294**, 256
- Reynolds R. J., 1989, *ApJ*, **345**, 811
- Reynolds R. J., 1991, in Bloemen H., ed., Vol. 144, The Interstellar Disk-Halo Connection in Galaxies. p. 67

- Reynolds R. J., Cox D. P., 1992, [ApJ](#), **400**, L33
- Reynolds R. J., Roesler F. L., Scherb F., 1973, [ApJ](#), **179**, 651
- Reynolds R. J., Hausen N. R., Tufte S. L., Haffner L. M., 1998, [ApJ](#), **494**, L99
- Rosales-Ortega F. F., Arribas S., Colina L., 2012, [A&A](#), **539**, A73
- Sánchez S. F., et al., 2012, [A&A](#), **538**, A8
- Seon K.-I., 2009, [ApJ](#), **703**, 1159
- Slavin J. D., Shull J. M., Begelman M. C., 1993, [ApJ](#), **407**, 83
- Sparre M., et al., 2015, [MNRAS](#), **447**, 3548
- Storchi-Bergmann T., Calzetti D., Kinney A. L., 1994, [ApJ](#), **429**, 572
- Thilker D. A., Braun R., Walterbos R. A. M., 2000, [AJ](#), **120**, 3070
- Thilker D. A., Walterbos R. A. M., Braun R., Hoopes C. G., 2002, [AJ](#), **124**, 3118
- Tinsley B. M., 1968, [ApJ](#), **151**, 547
- Tüllmann R., Dettmar R. J., Soida M., Urbanik M., Rossa J., 2000, [A&A](#), **364**, L36
- Vale Asari N., Couto G. S., Cid Fernandes R., Stasińska G., de Amorim A. L., Ruschel-Dutra D., Werle A., Florido T. Z., 2019, [MNRAS](#), **489**, 4721
- Vale Asari N., et al., 2020, [MNRAS](#), **498**, 4205
- Voges E. S., Walterbos R. A. M., 2006, [ApJ](#), **644**, L29
- Walterbos R. A. M., Braun R., 1994, [ApJ](#), **431**, 156
- Wang J., Heckman T. M., Lehnert M. D., 1997, [ApJ](#), **491**, 114
- Weedman D. W., 1977, [ARA&A](#), **15**, 69
- Weingartner J. C., Draine B. T., 2001, [ApJS](#), **134**, 263
- Wiener J., Zweibel E. G., Oh S. P., 2013, [ApJ](#), **767**, 87
- Wood K., Mathis J. S., 2004, [MNRAS](#), **353**, 1126
- Zaw I., Chen Y.-P., Farrar G. R., 2019, [ApJ](#), **872**, 134
- Zhang K., et al., 2017, [MNRAS](#), **466**, 3217
- Zurita A., Rozas M., Beckman J. E., 2000, [A&A](#), **363**, 9
- Zurita A., Beckman J. E., Rozas M., Ryder S., 2002, [A&A](#), **386**, 801

Appendix A: Emission line measurement

Appendix A.1: Cube preprocessing

Each individual spectrum of the cube, after being brought to the rest-frame, must be corrected for Milky Way extinction. The correction is carried out by multiplying each spectrum by a factor $10^{0.4a_\lambda}$, where a_λ is the extinction function of Fitzpatrick (1999), using the Python library *extinction.fitzpatrick99*⁷, that reads the $R_V = A_V/E(B - V)$ ratio (fixed at 3.1) and the total V-band extinction in magnitudes for each galaxy, obtained from Hyperleda. Values can be found in the table of BETIS characteristics online.

In this work we use CB07 (Bruzual 2007a,b) base spectra for the SSP models. The model spectra have a resolution of $R \sim 2000$ and 1λ of spectral sampling. Our observed spectra have $R \sim 3000$ and 1.25λ of spectral sampling, so the observed spectra must be resampled at 1λ . Performing a linear interpolation of every single spectra of the cubes resolve the conflict between the samplings.

After this steps, we obtain a new observed cube, rest-framed, resampled to $\Delta\lambda = 1 \text{ \AA}$ and corrected to Milky Way extinction. This new resampled cubes are those using to perform the SSP fittings.

Appendix A.2: Single Stellar Population synthesis

A Single Stellar Population (SSP) synthesis (Tinsley 1968) consists in an estimation of the type of stellar populations, i.e., the masses, ages and metallicities, found in a galaxy, star cluster, or region of a galaxy based upon its spectra. The SSP synthesis is carried by the software STARLIGHT (Cid Fernandes et al. 2005), that fits an observed spectrum O_λ with a model M_λ which adds up N_* spectral components from a pre-defined set of base spectra. The synthetic model spectra that the program generates have the form

$$M_\lambda = M_{\lambda_0} \left(\sum_{j=1}^{N_*} x_j b_{j,\lambda} r_\lambda \right) \otimes G(v_*, \sigma_*) \quad (\text{A.1})$$

where $b_{j,\lambda}$ is the spectrum of the j th SSP normalized. r_λ is the reddening term, M_{λ_0} is the synthetic flux at the normalization wavelength, \otimes is the convolution operator, $G(v_*, \sigma_*)$ is a Gaussian distribution centred at velocity v_* and with dispersion σ_* , and \mathbf{x} is the population vector. Each component x_j ($j = 1, \dots, N_*$) represents the fractional contribution of the SSP with age t_j and metallicity Z_j to the model flux.

As previously mentioned, we use the CB07 base spectra for the fittings. The $N_* = 100$ SSPs comprises 3 metallicities, $Z = 0.2, 1$ and $2.5Z_\odot$, and 15 ages from $t = 0.001$ to $t = 13$ Gyr. All SSPs are normalized to $1M_\odot$ at $t = 0$. Their spectra were computed with Padova-2004 evolutionary tracks models, and Chabrier (2003) IMF ($0.1M_\odot < M < 100M_\odot$).

The CB07 base comprises SSPs with the same metallicities and age range than the BC03 base (Bruzual & Charlot 2003). The difference between them are the TP-AGB spectra that CB07 adds in the base and the use of MILES-2007 evolutionary tracks models instead of Padova-2004.

For the preliminary results in this work, we perform the SSP fitting with the CB07 base spectra.

STARLIGHT takes as input the wavelengths (λ), the observed spectrum (O_λ , resampled, rest-framed and corrected by

MW extinction), the errors (e_λ), a base-master file with the SSPs, and a mask file. The mask file contains the regions of the spectra that we do not want to model with STARLIGHT, like emission lines, artefacts and holes in O_λ . One STARLIGHT is running, it will build the synthetic spectra M_λ of the form of equation (A.1) and will find the one that best fits the observed O_λ . The outputs files contains the population mixture of the best fit; the x_j , Z_j , t_j , $(L/M)_j$, stellar masses and the percentage of each component, among the synthetic spectrum M_λ .

Once we run STARLIGHT with all spaxels of our MUSE datacubes (~ 100.000 spectra per cube), we can build a 'nebular gas' or 'residue' datacube of the form $O_\lambda - M_\lambda$, containing the nebular emission of the object (see figure A.1).

Then, using the Python MPFIT⁸ module, we perform a Gaussian fitting around the emission lines of interest for all the spaxels of the nebular gas cube. This module performs a multipeak Gaussian fit for each individual line, with $\sigma = FWHM_i / (2\sqrt{2\ln 2})$, being $FWHM_i$ the MUSE initial Full Width Half Maximum, corresponding to 3 \AA . The module search the peak of the line in a 10 \AA (200-300 km/s) range centred in a central wavelength λ_c and performs the Gaussian fit in a range between $0.5\sigma - 2\sigma$. The flux of the i, j spaxel for the λ line is then defined as $f_{i,j}(\lambda) = \sqrt{2\pi} I_{peak}$, and I_{peak} the peak of the Gaussian fit (see figure A.2).

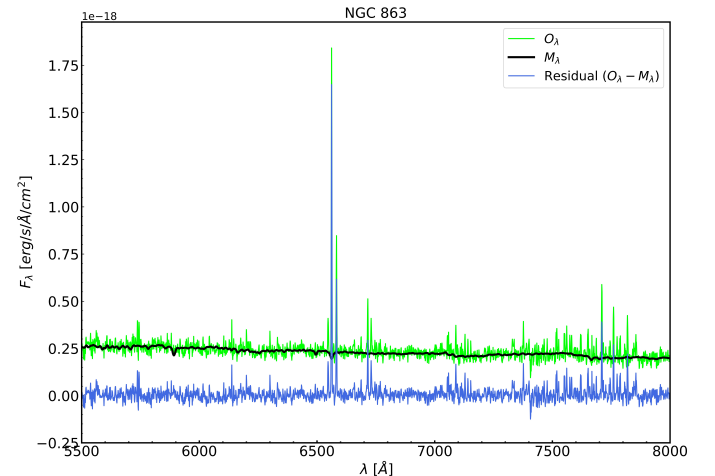


Fig. A.1. Example of a SSP fitting for a simple spaxel of the galaxy NGC 863. The observed, rest-framed and resampled spectrum is colored in green. The black spectrum is the best fit synthetic spectrum we get from the STARLIGHT SSP fitting, and the blue spectrum is the nebular emission of the spaxel, obtained from the residue of the fit, subtracting the synthetic spectrum to the observed.

⁷ <https://extinction.readthedocs.io/en/latest/index.html>

⁸ <https://github.com/segasai/astrolibpy/blob/master/MPFIT/MPFIT.py>

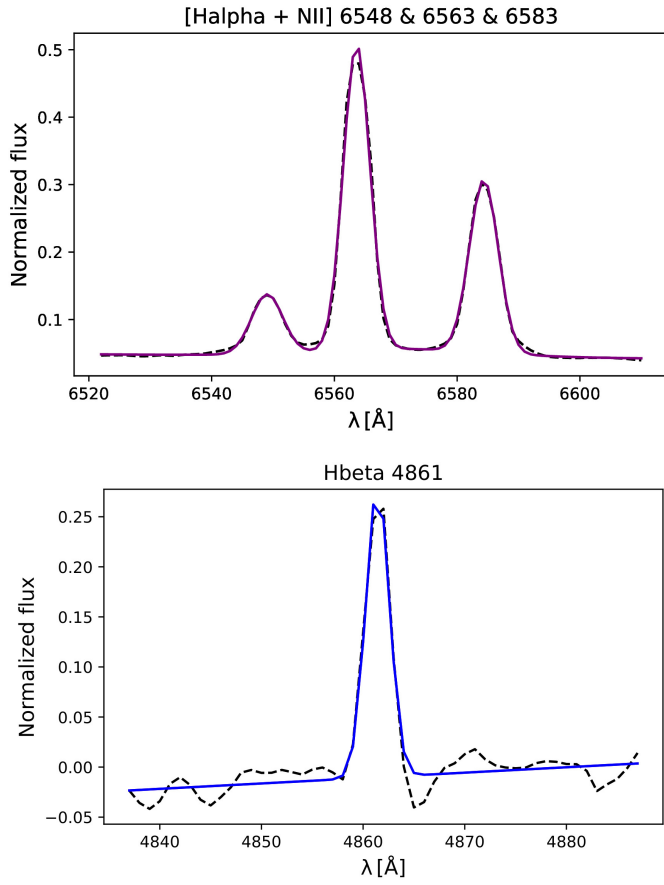


Fig. A.2. Top: Example of the multipeak fitting of $H\alpha$ and $[N II]$ lines. The purple curve is the Gaussian curve fitted. Bottom: Example for $H\beta$. Blue curve is the Gaussian curve fitted. In both cases, black dashed line is the input spaxel spectrum.